

# Multiscale Excitations in the Diluted Two-dimensional $S = 1/2$ Heisenberg Antiferromagnet

Liuyun Dao,<sup>1</sup> Hui Shao,<sup>2,3,\*</sup> and Anders W. Sandvik<sup>4,5,†</sup>

<sup>1</sup>*School of Physics and Astronomy, Beijing Normal University, Beijing 100875, China*

<sup>2</sup>*Center for Advanced Quantum Studies, School of Physics and Astronomy, Beijing Normal University, Beijing 100875, China*

<sup>3</sup>*Key Laboratory of Multiscale Spin Physics (Ministry of Education), Beijing Normal University, Beijing 100875, China*

<sup>4</sup>*Department of Physics, Boston University, 590 Commonwealth Avenue, Boston, Massachusetts 02215, USA*

<sup>5</sup>*Beijing National Laboratory for Condensed Matter Physics and Institute of Physics, Chinese Academy of Sciences, Beijing, 100190, China*

(Dated: August 14, 2024)

We study the excitation spectrum of the  $S = 1/2$  Heisenberg model on the randomly diluted square lattice by stochastic analytic continuation of imaginary-time correlations obtained by quantum Monte Carlo simulations in the low-temperature limit. Focusing on relatively low dilution fractions,  $p = 1/16$  and  $p = 1/8$ , the dynamic structure factor  $S(\mathbf{q}, \omega)$  exhibits a strongly damped magnon peak with anomalous dispersion near  $\mathbf{q} = (0, 0)$  and  $(\pi, \pi)$ , a non-dispersive low-energy peak from localized excitations, and a second dispersive peak within the continuum connecting these two features. A magnon with anomalous logarithmic dispersion, close to our result, was predicted in spin wave and  $T$ -matrix theory [A. Chernyshev et al., Phys. Rev. B **65**, 104407 (2002)], with the quasiparticle description breaking down at the low localization energy. However, no intermediate dispersive mode was predicted. Analyzing spectral functions in real space for individual vacancy realizations by energy tomography, we find that these excitations are concentrated on a subset of the spins adjacent to vacancies, with fewer spins involved as the energy is lowered. We argue that the low-energy excitations are those of a sparse random network of effective moments at a fraction of the vacancies. In the case of the magnon, there is a shift in spectral weight distribution, from the spins away from vacancies at high energy to those adjacent to vacancies at lower energy. We also analyze the Anderson quantum rotor excitation at  $\omega \propto N^{-1}$  (with  $N = L^2$  the system size), which in the clean system is visible in  $S(\mathbf{q}, \omega)$  only at  $\mathbf{q} = (\pi, \pi)$  but spreads through the entire Brillouin zone due to the lack of translational invariance when  $p > 0$ . Beyond weight close to  $\mathbf{q} = (0, 0)$  and  $(\pi, \pi)$ , which we explain by local sublattice imbalance within a classical dimer-monomer model, there is also intricate structure arising from correlated singlet fluctuations, which we demonstrate by enhancing said fluctuations with four-spin couplings in the Hamiltonian. The features in momentum space reflect spatially nonuniform breaking of the spin rotation symmetry and should be experimentally observable with elastic neutron scattering on layered quantum antiferromagnets doped with nonmagnetic impurities. All the  $\omega > 0$  excitations should be observable by inelastic neutron scattering. Technically, our work demonstrates that surprisingly complex spectral information can be obtained from quantum Monte Carlo data, despite the “ill-posed” numerical analytic continuation problem.

## I. INTRODUCTION

Two-dimensional (2D) Heisenberg antiferromagnets doped with nonmagnetic impurities (e.g., replacing Cu by Zn in copper oxides) exhibit interesting phenomena in experiments [1–6] that have inspired extensive analytical [7–18] and computational [17, 19–30] research on diluted  $S = 1/2$  Heisenberg models. Many works have focused on systems at and close to the classical percolation point (up to which the system remains long-range ordered [21]), where interplay of geometrical and quantum fluctuations lead to unusual low-energy excitations [27–30]. An important aspect here is the local sublattice imbalance caused by random dilution of a bipartite lattice. It was recently argued, based on classical dimer-

monomer models (which can explain some aspects of the excitations at the percolation point [27, 28]) that sublattice imbalance may also lead to profound changes in the excitations of the Néel state even at low dilution [31]. This proposal, along with previous detailed, but so far untested predictions from spin wave and  $T$ -matrix theory [9, 10, 14, 15], motivates us to carry out quantum Monte Carlo (QMC) studies of the 2D Heisenberg model in the low-temperature limit at relatively low dilution fractions,  $p = 1/16$  and  $1/8$ .

We compute imaginary-time correlation functions that we analytically continue for the frequency ( $\omega$ ) and momentum ( $\mathbf{q}$ ) resolved dynamic structure factor  $S(\mathbf{q}, \omega)$  using the stochastic analytic continuation (SAC) [32] method. In addition to studying the  $\mathbf{q}$  and  $\omega$  dependence of the disorder averaged  $S(\mathbf{q}, \omega)$  for system sizes  $N = L^2$  with  $L$  up to 64, we also compute real-space distributions  $S(\mathbf{r}, \omega)$  of spectral weight in individual vacancy realizations. Tomographic analysis of  $S(\mathbf{r}, \omega)$  in

\* huishao@bnu.edu.cn

† sandvik@bu.edu

different energy windows provides us with direct insights into the nature of different types of excitations.

Our numerical calculations, in synergy with previous analytical results, lead to an intriguing picture of the excitations of the diluted antiferromagnet, which apart from its direct experimental relevance also presents a key paradigmatic “strong disorder” problem in quantum many-body theory (as discussed at length in Ref. 15). Unbiased numerical calculations of dynamic spectral functions pose formidable challenges in their own right. We here report unprecedented resolution of the dynamic structure factor at multiple energy scales, identifying six different spectral attributes in  $S(\mathbf{q}, \omega)$  that can be assigned to specific types of excitations. We here first summarize these excitation modes.

For all  $\mathbf{q}$ , a very sharp peak is present at  $\omega \propto 1/L^2$  that originates from the lowest Anderson quantum rotor mode related to the breaking of the spin-rotation symmetry in the Néel state. There is another dispersionless peak at  $\omega > 0$ , predominantly arising from a very small fraction of spins adjacent to vacancies. This localized mode is followed by a dispersing peak that we identify as narrow band of damped excitations, likewise involving mainly spins next to vacancies but a much larger subset as compared to the localized excitations. A band of damped magnons follows, with the character of the magnons changing from low to high energy. At low energy, the spectral weight is large on all the spins next to vacancies, while at high energy, with  $\mathbf{q}$  close to the magnetic zone boundary, there is much less spectral weight on those spins and more within the uniform bulk patches between the vacancies. Finally, the magnon peak is always followed by a very large multimagnon tail.

In the remainder of this Introduction, we briefly review the previous analytical results in Sec. IA, and in Sec. IB we present more details on our results, their interpretations, and the how they compare with the previous predictions. We outline the rest of the paper in Sec. IC.

### A. Previously predicted excitations

According to the most sophisticated spin wave and  $T$ -matrix analysis [15], the excitation spectrum should indeed exhibit a multiscale structure, with strongly damped spin waves renormalized down in energy by the disorder at low energy, close to  $\mathbf{q} = (0, 0)$  and  $(\pi, \pi)$ . There is a localized (dispersionless) mode at a very low  $p$  dependent energy,  $\omega_{\text{loc}} \sim e^{-\pi/4p}$ . On approaching this energy, the assumption of the spin waves propagating in a disorder averaged medium becomes invalid, and the dynamics is then completely incoherent, with no well defined quasi particle. Our results partially confirm this picture but also, as summarized above and with more details to follow in Sec. IB, demonstrate an even richer excitation spectrum.

The available theoretical predictions are detailed [15], with the anomalous dispersion at small  $p$  and momenta

close to  $(0, 0)$  and  $(\pi, \pi)$  given in units of  $J$  by

$$\omega_{\text{ano}}(k) = c_0 k [1 + 2p \ln(k/\pi)], \quad (1)$$

where  $k$  is the momentum relative to one of the above two  $\mathbf{q}$  points,  $c_0$  is the spin wave velocity of the clean 2D Heisenberg model, and the lattice constant is set to unity. This dispersion relation should break down at energy  $\omega_{\text{loc}}$ , where the localized states produce a sharp peak in  $S(\mathbf{q}, \omega)$  for all  $\mathbf{q}$ . An essentially featureless spectral function was predicted between the localization and magnon peaks when the two are individually discernible. The two features merge when  $\omega_{\text{ano}}(k) \rightarrow \omega_{\text{loc}}$ , i.e., the magnons localize at this energy.

The anomalous magnon is also significantly damped, with the peak in  $S(\mathbf{q}, \omega)$  having a width of order  $pk$ . Further, the anomalous dispersion should only apply at energies below  $\omega \approx J$ , and a separate band of excitations, similar to the spin waves in the undiluted system, remains for  $\mathbf{q}$  close to the magnetic zone boundary (where  $\omega \approx 2J$ ). In some parts of the Brillouin zone (BZ), this mode coexists with the anomalous magnons at lower energy. The exact nature of the cross-over or coexistence between the two types of magnons is not clear, because crucial interactions when the spin waves resonate with the local impurity modes were not taken into account.

Technically, the calculation leading to these predictions [15] is based on mutually noninteracting spin waves (linear spin wave theory) within which the single-vacancy system is first solved exactly. The multi-vacancy system is then treated perturbatively within the  $T$ -matrix formalism, summing all diagrams involving single impurity scattering. Disorder averaging is carried out before evaluating  $S(\mathbf{q}, \omega)$ , which effectively implies that the excitations are those of an impurity-averaged bulk medium. The predictions should be valid at low dilution and low energy; specifically, when single-impurity scattering dominates. However, it is a priori not clear whether collective impurity effects “washed out” by the formalism may possibly leave out some excitations or create artificial features, as indeed demonstrated by our numerical results summarized above and presented in more detail next.

### B. Computational results and their interpretation

Our numerical approach is complementary to the theory, in the sense that it is well suited for accessing excitations at small to moderate length scales and there are no approximations beyond the limitations of numerical analytic continuation (which we will argue are minor here). Because of practical restrictions in the system size in QMC simulations at extremely low temperatures (essentially in the ground state), here  $N = L^2$  spins with  $L \leq 64$ , we cannot reach momenta in the very close neighborhood of  $(0, 0)$  and  $(\pi, \pi)$ . We nevertheless identify long-wavelength features similar to those predicted, though not always with full quantitative agreement. As

already mentioned, we also demonstrate some qualitative discrepancies between theory and numerics.

We observe the dispersionless localized mode and extrapolate its energy to the thermodynamic limit for  $p = 1/8$ . The result,  $\omega_{\text{loc}} \approx 0.1$ , would require the factor  $A$  of the predicted peak energy [15]  $\omega_{\text{loc}} = Ae^{-\pi/4p}$  to be as large as 50, but the form may only strictly apply for much smaller  $p$ . At  $p = 1/16$ , we are not able to distinguish our extrapolated value from 0 within numerical uncertainties. At higher energy we observe the magnon peak, with dispersion relation  $\omega_{\text{mag}}(\mathbf{q})$  close to  $\omega_0(\mathbf{q})$  of the clean 2D Heisenberg model for  $\mathbf{q}$  at and close to the zone boundary, then dropping sharply in a way closely matching Eq. (1) when approaching  $(0, 0)$  and  $(\pi, \pi)$ .

The high-energy dispersion includes the characteristic drop relative to low-order spin wave theory at  $\mathbf{q} = (\pi, 0)$  [33, 34]. This  $(\pi, 0)$  anomaly in the clean 2D Heisenberg model has been identified as a precursor to spinon deconfinement [35–37]. Thus, our results indicate that this precursor survives also in the diluted system, which we explore further by adding the same four-spin interaction to the Heisenberg Hamiltonian as in Ref. 36.

In the spin wave theory the magnon in the diluted system is split into two branches at energies close to  $J$  [9, 15], but we always find a single peak in this energy range. The double peak may reflect an inability of the analytic theory to fully take into account interactions between the spin waves and the impurity modes [15]. Low-order spin wave theory in general also cannot quantitatively describe high-energy magnons and multi-magnon continua, which is most apparent in the  $(\pi, 0)$  anomaly, which in addition to the energy suppression also involves a significant multimagnon continuum at higher energy. In the diluted systems we find an even more prominent continuum, extending as high as to  $\omega \sim 5J$  over much of the BZ. Apart from the multimagnon tail, the magnon peak is always very broad, in qualitative agreement with the prediction of the width being proportional to  $pk$  at small  $k$ , with  $k$  defined after Eq. (1).

In contrast to the spin wave theory, we find a second dispersive peak in  $S(\mathbf{q}, \omega)$  at energies between the magnon and the localized mode—at about 20% of the magnon energy close to the zone boundary and smaller relative suppression close to  $\mathbf{q} = (0, 0)$  and  $(\pi, \pi)$ . The peak emerges systematically with increasing system size in the energy range where the analytic calculation [15] only produced a rather flat continuum.

We gain further insights into the nature of the two propagating modes by investigating the real-space ( $\mathbf{r}$ ) resolved local dynamic structure factor  $S(\mathbf{r}, \omega)$  for individual vacancy realizations. By conducting tomography of such functions in  $\omega$  space, i.e., separating contributions from different energy windows, we can clearly see that the low-energy propagating mode is concentrated on some of the spins adjacent to the vacancies. These spins interact with each other through the bulk medium, with an effective coupling that necessarily must be much weaker than the bare Heisenberg coupling  $J$ , thus qualitatively

explaining the reduced energy scale as compared to the magnon. Based on our real-space insights, we conjecture that the excitations are those of a random network of a subset of the spins adjacent to vacancies; thus we will refer to the low-energy dispersive mode as the random network mode and denote its energy  $\omega_{\text{rn}}(\mathbf{q})$ .

The magnons at the zone boundary occupy mainly the uniform patches of space between the vacancies. At the dilution fractions  $p$  considered here, the patches can typically accommodate several wave lengths at the highest energies, explaining the closeness of their (peak) energy  $\omega_{\text{mag}}(\mathbf{q})$  to  $\omega_0(\mathbf{q})$ , though the damping is very significant. At longer wave lengths, where the magnon drops below  $\omega_0(\mathbf{q})$ , to approximately  $\omega_{\text{ano}}(k)$  in Eq. (1) with a slightly renormalized velocity, the tomography informs us that both the spins at and between the vacancies are involved in the excitations, now with all the spins adjacent to vacancies carrying elevated spectral weight and the other spins having almost uniform but lower weight.

Thus, starting from the high energy magnons with energy close to  $\omega_0$ , the excitations mainly affect the spins within the patches between vacancies. Spectral weight is gradually transferred to all the spins at distance one lattice spacing from the vacancies as the magnons drop to the anomalous energy  $\omega_{\text{ano}}$ . When the energy is further reduced to that of the random network mode at  $\omega_{\text{rn}}$ , the spectral weight away from the vacancies is further depleted and also removed from many of the spins neighboring vacancies, leaving a rather small subset of spins that carry large spectral weight. There is a sharp further reduction in the number of participant spins when the energy drops toward  $\omega_{\text{loc}}$ .

All the above excitations should be observable by inelastic neutron scattering experiments in 2D quantum antiferromagnets doped with nonmagnetic impurities, e.g., cuprate oxides with Cu substituted by Zn or Mg. A potentially even better starting point may be  $\text{Cu}(\text{DCOO})_2 \cdot 4\text{D}_2\text{O}$ , if it also can be successfully doped with Zn or Mg—we are not aware of any attempts so far. The pristine system is currently regarded as the best realization of the 2D Heisenberg model, with the measured inelastic neutron scattering cross section being in very close agreement with that of the model [35, 36].

In addition to all the  $\omega > 0$  excitations, in the finite systems studied here, the spin-rotation symmetry is not broken and collective excitations are expected at energy scaling as  $1/N$ —the Anderson tower of quantum rotor states that become degenerate in the thermodynamic limit and facilitate the broken symmetry. These excitations are not included in spin wave and related calculations starting from a state with broken symmetry, but they are important as a probe of the nature of the ground state. In the case of a pristine lattice, the rotor states exist at wave-vectors  $\mathbf{q} = (0, 0)$  (even total spin  $S$  modes) and  $(\pi, \pi)$  (odd  $S$  modes), but only the  $S = 1$  state at  $(\pi, \pi)$  contributes to  $S(\mathbf{q}, \omega)$ .

In the diluted system, where translational symmetry is broken, the weight of the rotor state in  $S(\mathbf{q}, \omega)$  spreads

out over momentum space in a way reflecting specific large-scale nonuniformities in the zero-energy fluctuations of the Néel order. We find an interesting structure of the  $\mathbf{q}$  dependent rotor weight that should be experimentally visible in elastic neutron scattering through broadening of the magnetic  $(\pi, \pi)$  Bragg peak and spectral weight moving to other parts of the BZ, including a peak forming around  $(0, 0)$ .

Peaks of rotor weight close to  $\mathbf{q} = (0, 0)$  and  $(\pi, \pi)$  can be qualitatively explained by a classical dimer-monomer model, which was previously used to study effects of local sublattice imbalance in  $S = 1/2$  Heisenberg antiferromagnets at the percolation point [28, 29, 38, 39], and also in other fractal clusters [38, 39]. Beyond the two peaks in the BZ, there are other weak variations of the rotor weight as a function of  $\mathbf{q}$  that are not explained by classical sublattice imbalance. We will show that a minimum at  $\mathbf{q} = (\pi/2, \pi/2)$  originates from a tendency of resonating dimer singlets to form local columnar correlations, as a precursor to a long-range ordered valence-bond solid state existing in an extended model space. We find support for this scenario by including a four-spin interaction  $Q$  in the Hamiltonian (the  $J$ - $Q$  model [40]), which further depletes the rotor modes close to  $\mathbf{q} = (\pi/2, \pi/2)$  as a consequence of correlated singlet fluctuations—the precursor to spinon deconfinement.

A recent comprehensive mathematical and computational study of the dimer-monomer model at low dilution found a novel type of monomer percolation phenomenon in the limit of low dilution [31]. It was proposed, without details, that some aspects of the low-energy excitations of the diluted Heisenberg model could reflect this percolation point  $p_c$ , especially in 3D systems where  $p_c > 0$  but perhaps also in 2D, where  $p_c = 0$ . Though, as mentioned above, in the rotor excitation we find signatures of sublattice imbalance as modeled by the dimer-monomer model, a possible relationship between monomer percolation and the  $p \rightarrow 0$  delocalization predicted in the  $T$ -matrix theory is less clear. We do find compelling evidence from our tomographic approach of the localized excitations also being tied to spins in the monomer rich regions. We will discuss how the length scale  $\propto e^{\pi/4p}$  in the spin wave theory [15] may be compatible with power law divergence of a monomer correlation length in the effective dimer-monomer description [31].

### C. Outline

The rest of the paper is organized as follows: In Sec. II we introduce the quantum spin models and also the classical dimer-monomer model that we use to qualitatively understand some of our results for the rotor excitations. We also provide tests of the SAC method by studying small systems that are amenable to exact Lanczos diagonalization. In Sec. III we present our results for the disorder averaged  $\mathbf{q}$  dependent and local dynamic structure factor, and also for the real-space resolved spectral

function of individual vacancy realizations. In Sec. IV we further analyze the way the quantum rotor contributions spread out in the BZ by the disorder. In Sec. V we present complementary results for the  $J$ - $Q$  model that are helpful for interpreting the rotor weight distribution. We conclude in In Sec. VI with a brief summary and further discussion of our results. Auxiliary results supporting our conclusions are presented in three appendices.

## II. MODELS AND METHODS

### A. Diluted quantum antiferromagnets

The  $S = 1/2$  Heisenberg model diluted by static vacancies is defined by the Hamiltonian

$$H_J = J \sum_{\langle ij \rangle} n_i n_j \mathbf{S}_i \cdot \mathbf{S}_j, \quad (2)$$

where  $\langle ij \rangle$  denotes nearest neighbors on the 2D square lattice and  $n_i = 1$  and  $n_i = 0$  for spins and vacancies, respectively. We set the exchange constant to  $J = 1$  and define the doping fraction  $p = N_0/N$ , where  $N_0$  is the number of randomly distributed vacancies in the canonical ensemble and  $N = L^2$  is the number of lattice sites. The classical percolation point above which there is no connected cluster of size  $\propto N$  is  $p_c \approx 0.407$ , and the system remains Néel ordered up to this point (with the fractal percolating cluster being ordered) [21]. We here consider  $p \ll p_c$  and mainly focus on the case of  $N_0/2$  vacancies on each of the two sublattices. In Appendix A we provide results showing no substantial differences for systems without this restriction.

We will also discuss some aspects of a system with an added four spin interaction, which when strong leads to a quantum phase transition from the Néel ground state to a columnar valence-bond solid [40]. In the presence of vacancies, this  $Q$  interaction is

$$H_Q = -Q \sum_{\langle ijkl \rangle} n_i n_j n_k n_l (\frac{1}{4} - \mathbf{S}_i \cdot \mathbf{S}_j)(\frac{1}{4} - \mathbf{S}_k \cdot \mathbf{S}_l), \quad (3)$$

where  $\langle ijkl \rangle$  corresponds to sites on a  $2 \times 2$  plaquette with  $ij$  and  $kl$  forming opposite edges (with both vertical and horizontal orientation). The  $J$ - $Q$  Hamiltonian is  $H = H_J + H_Q$  and we here use  $J + Q = 1$  as the energy scale. In addition to the Heisenberg model with  $Q = 0$ , we will consider  $Q/J = 1$  and  $Q/J = 2$ , where the system is still in the Néel state, far from the transition point at  $Q/J \approx 22$ , but already exhibits large changes in the excitation spectrum (as found in the case of the clean system in Ref. 36). The purpose of  $Q > 0$  here is to amplify effects that we argue arise from local columnar dimer fluctuations already at  $Q = 0$ .



## B. Spectral functions

Our main aim here is to investigate the excitations of the system through the dynamic spin structure factor  $S(\mathbf{q}, \omega)$ , where  $\omega$  is the excitation energy in units of  $J = 1$  for the Heisenberg model (and later  $J+Q = 1$  in the  $J$ - $Q$  model) and the momentum (wave vector) is  $\mathbf{q} = (q_x, q_y)$ , with  $(q_x, q_y) = 2\pi(k_x, k_y)/L$  and  $k_x, k_y = 0, \dots, L-1$ .

For any bosonic operator  $O$ , the spectral function at temperature  $T = 0$  can be written in the basis of eigenstates  $|n\rangle$  and eigenvalues  $E_n$  of the Hamiltonian as:

$$S(\omega) = \pi \sum_n |\langle n|O|0\rangle|^2 \delta(\omega - E_n + E_0). \quad (4)$$

For the dynamic spin structure factor  $S(\mathbf{q}, \omega)$  of the spin-rotation invariant Heisenberg model the operator can be taken as the Fourier transform of the spin- $z$  operator:

$$O_{\mathbf{q}} = \frac{1}{\sqrt{N}} \sum_{\mathbf{r}} e^{-i\mathbf{q}\cdot\mathbf{r}} S_{\mathbf{r}}^z, \quad (5)$$

where  $\mathbf{r} = (x, y)$  is the site coordinate with unit lattice constant. This operator produces only  $S = 1$  excitations when acting on the  $S = 0$  ground state of a clean  $L \times L$  system with even  $L$ . However, the diluted system can contain clusters with unequal occupation of the two sublattices, which have ground states with  $S > 0$ . The excitations then can have spin  $S + 1$  or  $S - 1$  relative to the ground state  $S$ . Our methods automatically perform the proper spin rotational averaging for ground states of any  $S$ . Since we are working at low dilution, the spectral functions are completely dominated by one large connected cluster.

While  $S(\mathbf{q}, \omega)$  can be computed for small systems using Lanczos exact diagonalization [41] (as we will also do), for larger systems it is not possible to obtain exact results. Here we compute the corresponding imaginary-time dependent correlation functions using QMC simulations on large lattices and perform numerical analytic continuation to real frequency.

The imaginary-time correlation function is

$$G(\mathbf{q}, \tau) = \langle O_{-\mathbf{q}}(\tau) O_{\mathbf{q}}(0) \rangle, \quad (6)$$

where  $O(\tau) = e^{\tau H} O e^{-\tau H}$  and its relationship to the dynamic structure factor is

$$G(\mathbf{q}, \tau) = \frac{1}{\pi} \int_0^\infty S(\mathbf{q}, \omega) e^{-\tau\omega}. \quad (7)$$

It is customary to define  $S(\mathbf{q}, \omega)$  with the full spin operator  $\mathbf{S}_{\mathbf{r}}$  instead of just the  $z$  component in Eq. (5), which we accomplish here by multiplying our QMC computed  $G(\mathbf{q}, \tau)$  by 3. In most cases the overall normalization will not be of importance.

We perform the QMC calculations of  $G(\mathbf{q}, \tau)$  with the Stochastic Series Expansion (SSE) method [42, 43] at sufficiently low  $T$  to converge to the ground state. For

efficient evaluation of correlations in imaginary time, we use the method of exact ‘‘time slicing’’ [44] (see Ref. 45 for other approaches and the relationship to conventional path integrals), with each slice of width  $\Delta_\tau$  expanded to all contributing orders. The space-time correlations can then be easily computed with the states separated by the operators corresponding to an integer number  $n$  of slices, whence  $\tau \in \{n\Delta_\tau\}$ . Since there are, as we will see, excitations with energy scaling as  $L^{-2}$  and our goal is to resolve these, we take the inverse temperature as high as  $\beta = 4L^2$  for  $L \leq 64$ . Disorder averages are computed over at least 1000 random vacancy samples.

## C. Stochastic analytic continuation

We employ the SAC method [32] to invert Eq. (7) for  $S(\mathbf{q}, \omega)$ . We here briefly describe how we apply the method to the particular model discussed here and also provide test comparing results for small systems with exact Lanczos calculations.

For a set of imaginary times  $\tau_i = 1, \dots, N_\tau$ , an SSE simulation provides an unbiased statistical estimate  $\bar{G}_i = \bar{G}(\tau_i)$  of the correlation function, where here we suppress the momentum label  $\mathbf{q}$  for simplicity and include it below only when presenting results. Importantly, the statistical errors of different data points  $i$  are correlated [46], which has to be properly taken into account for the SAC method to be statistically sound. With the SSE data divided into bins indexed by  $b = 1, 2, \dots, N_B$ , the covariance matrix is given by:

$$C_{ij} = \frac{1}{N_B(N_B - 1)} \sum_{b=1}^{N_B} (G_i^b - \bar{G}_i)(G_j^b - \bar{G}_j), \quad (8)$$

where  $G_i^b$  denotes the mean of the data in bin  $b$  and  $\bar{G}_i$  is the average over all  $b$ . The diagonal elements of the covariance matrix  $C$  are the conventional variances (squares of the standard statistical errors),  $\sigma_i^2 \equiv C_{ii}$ .

With the expected presence of excitations at very low energy, we need correspondingly long imaginary times. It is then neither feasible nor necessary to use a dense linear grid of  $\tau$  points, and we instead use a linear grid only for  $\tau \in [0, 2]$  at spacing  $\Delta_\tau = 0.1$ , thereafter switching to values of the form  $\tau \propto n^2 \Delta_\tau$ , with  $n$  such that  $\tau > 2$  and the constant of proportionality chosen such that of the order 100-200 time points are typically computed. As discussed further below, not all of these data points may be used as input in the SAC, because of an error-determined cut-off imposed on the maximum time and also because the set may be pruned to ensure a stable covariance matrix.

Given a proposal for  $S(\omega)$ , a corresponding set of values  $\{G_i\}$  can be computed by Eq. (7). The deviation of this set from the SSE output set  $\{\bar{G}_i\}$  is quantified in the

standard way by the "goodness-of-fit"

$$\chi^2 = \sum_{i=1}^{N_\tau} \sum_{j=1}^{N_\tau} (G_i - \bar{G}_i) [C^{-1}]_{ij} (G_j - \bar{G}_j), \quad (9)$$

which after diagonalizing and transforming everything to the basis of eigenvectors of the covariance matrix takes the conventional uncorrelated form

$$\chi^2 = \sum_{i=1}^{N_\tau} (G_i - \bar{G}_i)^2 / \epsilon_i^2, \quad (10)$$

where  $\epsilon_i^2$  are the eigenvalues of  $C$  (i.e.,  $\epsilon_i$  are the standard deviations of the independently fluctuating stochastic modes) and the transformed  $G_i$  and  $\bar{G}_i$  are implied.

In SAC, the spectral function is normally parametrized using a large number of  $\delta$  functions located at frequencies  $\omega_i$  and with positive semi-definite amplitudes  $a_i$ . The parameter space  $\{a_i, \omega_i\}$  is treated as that of a statistical mechanics problem with  $\chi^2$  corresponding to the energy, sampling according to the Boltzmann-like distribution,

$$P(S) \propto \exp\left(-\frac{\chi^2}{2\Theta}\right), \quad (11)$$

at a fictitious temperature  $\Theta$ . For  $\Theta \rightarrow 0$ , this procedure reaches a minimum goodness-of-fit  $\chi_{\min}^2 > 0$  ( $\chi_{\min}^2 = 0$  being possible only if negative amplitudes are allowed), which is taken as a proxy for an effective number of degrees of freedom  $N_{\text{dof}}$  of the fit, from the fact that the expected value of  $\chi_{\min}^2$  (in a fit to a valid function) equals  $N_{\text{dof}}$  in the  $\chi^2$  distribution. The temperature  $\Theta$  is then adjusted so that

$$\langle \chi^2(\Theta) \rangle = \chi_{\min}^2 + a\sqrt{2\chi_{\min}^2}, \quad (12)$$

where  $2\chi_{\min}^2$  acts as a proxy for the variance of  $\chi_{\min}^2$  according to the  $\chi^2$  distribution. Here the factor  $a$  should be of order 1 (normally we take  $a \approx 0.25 \sim 0.5$ ), which corresponds to a statistically good average fit, with  $\langle \chi^2 \rangle$  falling within a standard deviation of the smallest goodness-of-fit expected, while avoiding overfitting for essentially the same reason. This  $\Theta$  criterion is discussed in detail in Ref. 32 and was recently further motivated in Ref. 47. The sampled spectrum is collected in the form of a histogram with bin width adjusted according to the energy scales appearing in the spectrum.

The SAC method is equivalent to the conventional Maximum-Entropy [46] method (MEM) under certain conditions (essentially for a very large number of  $\delta$  functions and with the entropic weighting in the MEM adjusted so that  $\chi_{\text{MEM}}^2 = \langle \chi_{\text{SAC}}^2 \rangle$ ) [32], but effectively with a different form of the entropy when sampling the spectrum in the space of both amplitudes and frequencies of the  $\delta$  functions (while the conventionally used Shannon entropy in the MEM is realized when sampling only the frequencies of equal-weight  $\delta$  functions) [32, 48]. It

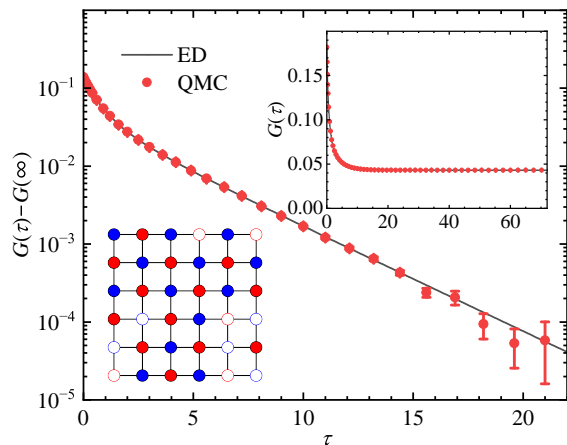


FIG. 1. SSE computed imaginary-time correlation function at  $\mathbf{q} = (\pi/3, 0)$  for the  $6 \times 6$  lattice in the inset, where there are five vacancies on each sublattice (the sublattices being indicated by red and blue, with spins and vacancies shown as solid and open circles, respectively). One of the spins (the rightmost one on the second row from the bottom) of the periodic lattice is isolated from the rest of the system, which forms a connected cluster. Because of the ground state degeneracy of this system,  $G(\mathbf{q}, \tau)$  does not decay to zero at large  $\tau$ , as seen in the inset. After subtracting the large- $\tau$  constant, the decay is exponential, as shown in the main figure, with the asymptotic exponential decay reflecting the gap, here  $\Delta = 0.309$ , of the large connected cluster. The curves show the corresponding exact results from Lanczos diagonalization.

has been shown that the fidelity of the method is often (but now always [47]) better than the conventional MEM when also the amplitudes are sampled [32] (a SAC parametrization first suggested by Beach [49]), as we do here.

For a connected spin cluster with equal number of sites on the two sublattices, the ground state is a singlet and  $G(\tau)$  decays to zero as  $\tau \rightarrow \infty$ . However, in systems randomly diluted with vacancies there will inevitably be some clusters with unequal sublattice occupation; the most common case being a single isolated spin, which also causes an opposite imbalance in the remaining large cluster. These imbalanced clusters lead to ground state degeneracies (finite total spin of the ground state of odd-sized clusters, as already discussed above in Sec. II B) and, accordingly,  $G(\tau)$  approaches a nonzero constant for large  $\tau$ . This behavior corresponds to a  $\delta$  function at  $\omega = 0$  in frequency space, which we omit by removing the large- $\tau$  constant from  $G(\tau)$  before performing the analytic continuation.

We illustrate this subtraction scheme for a  $6 \times 6$  system in Fig. 1, where there is a single isolated spin and the remaining large cluster also has an odd number of spins. The correlation function  $G(\mathbf{q}, \tau)$  at  $\mathbf{q} = (\pi/3, 0)$  is shown for  $\tau$  up to  $\beta/2$  in the inset, where the decay toward a nonzero constant is clear. After subtracting this constant, the asymptotic decay is exponential,  $G_{\mathbf{q}}(\tau) \propto e^{-\tau\Delta}$ , where in this case the gap is  $\Delta = 0.3090$ .

The SSE results agree with the exact  $G(\tau)$  for all  $\mathbf{q}$ , both before and after subtraction (with the same gap for all  $\mathbf{q}$  because of the lack of translation symmetry). The  $\omega = 0$  contribution can be added to the spectrum after the analytic continuation, but in most cases, at the dilution fractions considered here, it is very small and not clearly visible in the graphs presented below.

Though the maximum imaginary time value,  $\tau = \beta/2$  [when taking into account that  $G(\tau) = G(\beta - \tau)$  for a bosonic operator], is in principle as large as  $2N$  in our calculations,  $G(\tau)$  is typically dominated by statistical noise at these large time separations. In practice, we only use the  $\tau$  points at which the computed relative statistical error (conventional standard deviation), after subtraction of the possible constant, is less than 10%. This cut-off is reflected in the data in the main part of Fig. 1, where the largest  $\tau$  value is about 22 even though  $\beta/2 = 72$ , following our criterion  $\beta = 4N$  to ensure sufficient convergence to the ground state. As  $L$  increases, spectral features appear at lower energies and the largest  $\tau$  value increases accordingly. As an example, for  $L = 64$  the 10% criterion for the relative statistical error can correspond to time up to  $\tau \approx 4000$ , and we then include a total of  $N_\tau \approx 70$  elements in the SAC input set  $\{G(\tau_i)\}$ .

It should be pointed out here that the statistical error in  $G(\tau)$  has two sources: from the finite-length SSE runs for the individual vacancy samples and from sample-to-sample fluctuations. The latter are typically larger, and, therefore, our SSE runs are rather short, which is possible because the equilibration and autocorrelation times are short even for randomly diluted Heisenberg systems [21]. We can then generate a large number of vacancy samples for each  $L$  and  $p$ . We have not investigated the details of the error correlations from the two sources of fluctuations, but all covariance effects are taken properly into account collectively by the covariance matrix, which in our SAC approach is diagonalized for use in Eq. (10).

#### D. Tests on small systems

For small systems, e.g., the diluted  $6 \times 6$  lattice considered in Fig. 1, the dynamic structure factor can be directly computed in the form of Eq. (4) using Lanczos exact diagonalization. The number of contributing  $\delta$  functions is then small (at temperature  $T = 0$  in our study) and cannot be well approximated by any continuous function. A direct comparison with results obtained with the SAC method, where an essentially continuous average spectrum is produced, is then typically not very meaningful. However, the locations and amplitudes of the  $\delta$  functions depend significantly on the details of the vacancy realization, and  $S(\mathbf{q}, \omega)$  averaged over a large number of samples can therefore be well approximated by a smooth continuum (which, as we will see, still can contain very sharp peaks). We here use this approach to test the SAC method.

Results for  $L = 6$  obtained with both the Lanczos

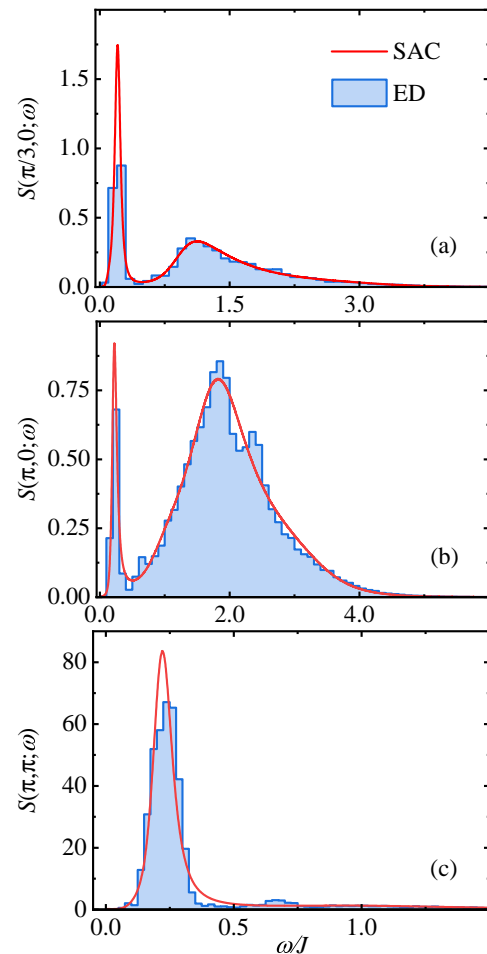


FIG. 2. Disorder averaged (2000 samples)  $S(\mathbf{q}, \omega)$  for system size  $L = 6$  diluted at  $p = 5/18$ . Results are shown at (a)  $\mathbf{q} = (\pi/3, 0)$ , (b)  $\mathbf{q} = (\pi, 0)$ , and (c)  $\mathbf{q} = (\pi, \pi)$ . The histograms represent the distribution of  $\delta$  functions in the exact expression Eq. (4) and the red curves are the results of the SAC method applied to SSE data.

method and SSE combined with SAC are displayed in Fig. 2 at three different momenta. The overall shapes of the Lanczos spectra, represented as histograms with suitable bin width, are remarkably well reproduced by the SAC method, except for small-scale structure that cannot realistically be reproduced by any numerical analytic continuation method applied to QMC data. In all cases, there is a sharp Gaussian like low-energy peak followed by a broad profile with non-trivial shape that depends on the momentum. For  $\mathbf{q} = (\pi/3, 0)$  and  $(\pi, 0)$  in Figs. 2(a) and 2(b), even the high-energy tails are almost flawlessly reconstructed by the SAC, while the much smaller second peak at  $\mathbf{q} = (\pi, \pi)$  in Fig. 2(c) cannot be well replicated because of its small relative spectral weight. The frequency resolution of peaks in analytic continuation of QMC data generally is better at low frequency, but the ability to resolve a specific detail also depends on its relative weight and other features present.

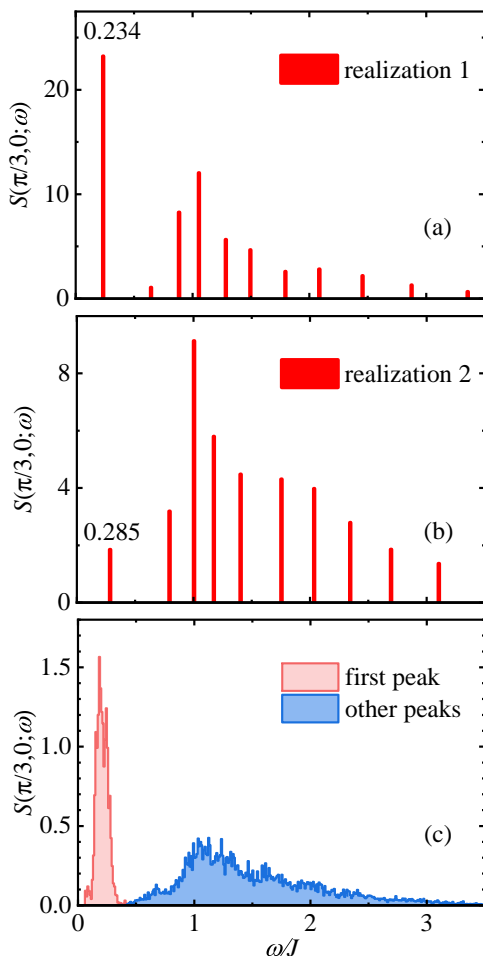


FIG. 3. Separation of low-energy peak and continuum. The exact form of  $S(\mathbf{q}, \omega)$  at  $\mathbf{q} = (\pi/3, 0)$  obtained with two different vacancy realizations from the same set as in Fig. 2 is shown in (a) and (b). The height of each bar corresponds to the squared matrix element in Eq. (4). The location of the energy of the lowest  $\delta$  function is indicated. The distribution of the energy of the lowest peak over 2000 samples is shown in red in (c), while the other contributions form the distribution shown in blue. There is practically no overlap between these two parts of the distribution. Here the data is the same as in Fig. 2(a) but the bin width in the histogram is smaller.

Below we will demonstrate that the lower peak in Fig. 2 develops with increasing system size into a  $\delta$  function at energy  $\omega \propto 1/N$ , reflecting the lowest excitation in what is known as the tower of Anderson quantum rotor states associated with the breaking of the  $O(3)$  symmetry of the Néel order parameter [43, 50, 51]. In a translationally invariant system, the  $S = 1$  rotor excitation of the ground state is present in  $S(\mathbf{q}, \omega)$  only at  $(\pi, \pi)$ . However, in a diluted system, where the momentum is not conserved, it spreads out over the entire BZ in a way reflecting nonuniformity in the  $\omega = 0$  long-range order. The energy of the rotor excitation must then be independent of  $\mathbf{q}$ , as indeed can be observed in Fig. 2 (note the different scales on the  $\omega$  axis for different  $\mathbf{q}$ ), where at

$\mathbf{q} = (\pi, \pi)$  the rotor peak contains the majority of the total spectral weight. We will show that the distribution of the spectral weight of the rotor mode, in both momentum space and real space, provides valuable information on the nature of the disordered Néel state.

For a finite system with rotationally averaged Néel ordered ground state (i.e., with the amplitude of the order parameter formed but the symmetry not broken), the lowest  $\delta$  function in the exact spectrum represents the rotor excitation. We can specifically confirm that the Gaussian like broadening of the low-energy peaks in Fig. 2 reflects the sample-to-sample fluctuations of the lowest peak in the exact spectra. Fig. 3(a) and Fig. 3(b) show the exact form Eq. (4) of  $S(\mathbf{q}, \omega)$  for two vacancy samples. Here the amplitudes of the  $\delta$  functions correspond to the heights of the bars at the locations  $\omega_n = E_n - E_0$ . Separating the contributions from the lowest  $\delta$  function and all other spectral weight, we see in Fig. 3 that the low-energy peak indeed arises exclusively from the lowest excitation of each sample. In Sec. III we will demonstrate that the width of the peak shrinks as the system size is increased while its location scales toward  $\omega = 0$  in the way expected for a rotor excitation.

For a cluster with equal number of spins on both sublattices, the ground state has total spin  $S = 0$  and the gap to the rotor states are of the form  $\Delta_S = S(S+1)/N$ . Only the  $S = 1$  state is visible in the dynamic spin structure factor because of the selection rules for the spin operators. The clusters formed in a diluted system typically have  $S > 1$  ground states, however, because of sublattice imbalance. In the example in Fig. 1, the ground states of the large connected cluster and the isolated spin both have spin  $S = 1/2$ , which implies that the ground state of the entire system is degenerate, with  $S = 0$  and  $S = 1$ . For larger systems with many isolated spins, where the main connected clusters can have ground state spin  $S > 1$ , there can be rotor states with both  $S+1$  and  $S-1$ . They will typically be very close to each other in energy, and we therefore still expect a single narrow rotor peak in the disorder averaged  $S(\mathbf{q}, \omega)$  at  $\omega \propto 1/N$ . The trivial  $\delta$ -peak resulting from ground state degeneracy are always removed from the imaginary-time correlation functions, as we explained above (Fig. 1).

Another potential complication for large systems is that there can also be relatively large isolated clusters of many spins in addition to the system spanning majority cluster. The emergent rotor states of these smaller clusters will have relatively high energy, and their contributions to  $S(\mathbf{q}, \omega)$  can then mix in with the other spectral features. However, at the low dilution fractions we consider here, isolated clusters of size larger than 1 are rare, and  $S(\mathbf{q}, \omega)$  is completely dominated by the largest cluster. We will see in Sec. III that a very clear separation forms with increasing system size between the low-energy rotor peak and the features at higher energy, even when those other features also move down in energy (in particular the localization peak), because the rotor peak narrows at the same time.

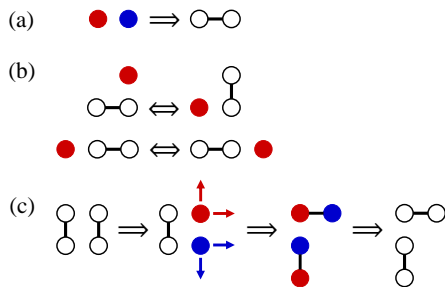


FIG. 4. Updating processes of the dimer-monomer model, with red (blue) circles representing sites of sublattice A (B). (a) Two nearest-neighbor monomers are annihilated, leading to a dimer. (b) Two different joint moves of a monomer and a dimer. Note that a given monomer can only move within one sublattice. (c) Breaking a dimer, then moving the two monomers until they can be annihilated with other monomers as in (a). Starting from a configuration of random dimers and monomers (where we place dimers first until no longer possible, whence the remaining sites are assigned as monomers), a series of updates are performed and the number of monomers gradually decreases by the process in (a). After a sufficiently long time the minimum number of monomers has been reached and the process continues for the purpose of collecting the spatial distribution of the remaining monomers. The update in (c) is strictly not needed for ergodicity, but it significantly speeds up the sampling after the minimum number of monomers has been reached.

### E. Dimer-monomer model

Even in a cluster with equal number of vacancies on the two sublattices, effectively localized spin degrees of freedom can emerge due to local sublattice imbalance. These effective moments are often referred to as “dangling spins”, though they can form at arbitrary locations of the lattice and are not necessarily (though often) obviously related to spins with very low coordination numbers; they are in many cases effectively spread out over large regions of the lattice. Such regions of average sublattice imbalance exhibit elevated magnetic response.

The formation of regions with net moments and their magnetic properties can often be surprisingly well modeled by a dimer-monomer model [28, 29, 31, 38, 39], where each monomer represents an “unpaired” spin and the dimers represent the background Néel order in which these spins reside. We will take this approach to explain some of the qualitative features of the distribution in the BZ of the weight of the rotor state in  $S(\mathbf{q}, \omega)$ , and also to discuss the potential connection between regions of local sublattice imbalance and localized excitations.

The monomers undergo stochastic (Monte Carlo) dynamics along with the dimers, and any pair of monomers occupying nearest-neighbor sites is eliminated (thus replaced by a dimer). The required ergodic updates of the dimer-monomer configurations are illustrated and further explained in Fig. 4. Once a steady state has been achieved, the spatial monomer distribution is accumu-

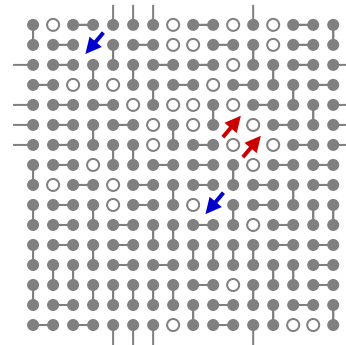


FIG. 5. A dimer-monomer configuration on a  $16 \times 16$  lattice, with vacancies indicated by open circles. Dimers connect nearest-neighbor sites and monomers are indicated by arrows, with red (up) and blue (down) corresponding to the A and B sublattices, respectively.

lated; for details see Ref. [28]. In Fig. 5 we show one configuration from such a simulation in which there are two monomers on each sublattice, with the sublattices associated with different spin- $z$  excess. Upon running the simulation, it is found that the “up” monomers are restricted to a small region of the lattice (one of them being completely isolated by surrounding vacancies), while the “down” ones can occupy most of the lattice but cannot reach the sites neighboring the monomers on the opposite sublattice, in which case they would be annihilated.

In a quasi-classical picture of the Néel state, the monomers are associated with spin up or down according to the sublattice within which they reside. They represent contributions to the magnetic properties of the ground state from local sublattice imbalance, while the dimers represent the background Néel state that is not considered within the dimer-monomer model. Thus, the monomer distribution represents changes relative to the perfect Néel state.

An important measure of nonuniformity in the diluted system is provided by the local spin susceptibility  $\chi_{\mathbf{r}}$ ,

$$\chi_{\mathbf{r}} = \int_0^\beta d\tau \langle S_{\mathbf{r}}^z(\tau) S_{\mathbf{r}}^z(0) \rangle, \quad (13)$$

where the integral can be performed analytically without approximations within the SSE method [52]. Previous studies have demonstrated a strong correlation between the spatial nonuniformity of the low-energy excitations and the monomer density at the 2D Heisenberg model at percolation point and other fractal clusters [28, 29, 38, 39]. We provide a similar example in the context of the 2D Heisenberg model at low dilution in Fig. 6. Here we clearly observe enhanced local magnetic response  $\chi_{\mathbf{r}}$  at the sites with high monomer density, though there are also sites with vanishing monomer density but nevertheless large response. Note again that the monomer density represents enhanced response relative to a background value in the regions without monomers.

In Sec. IV the purpose of studying the dimer-monomer



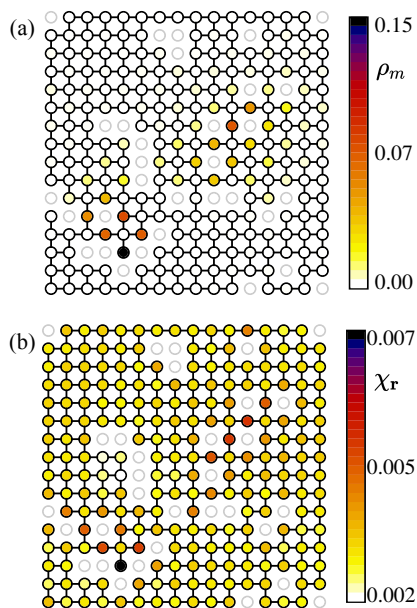


FIG. 6. Visualization of effective magnetic moments formed due to local sublattice imbalance in an  $L = 16$  system at dilution fraction  $p = 1/8$ . The dim circles not linked to other circles represent vacancies. (a) The monomer density obtained by sampling dimers and monomers according to the rules in Fig. 4. (b) The local spin susceptibility, Eq. (13), of the spin-1/2 Heisenberg model, Eq. (2).

model will be in the context of the weight distribution of the Anderson rotor excitation in the BZ, where we will similarly find that some aspects of the nonuniform symmetry breaking can indeed be explained by local sublattice imbalance, modeled by monomers, while there is also structure not captured by the clearly very simplistic classical description.

The monomer regions may also provide a bridge between the dimer-monomer model and the localized modes at large length scale for low  $p$ , though the quantitative match between the pictures is not obvious, as we will discuss below in Sec. III D and further in Sec. VI.

### III. DYNAMIC STRUCTURE FACTOR

In Sec. III A we present our results for  $S(\mathbf{q}, \omega)$  computed on system sizes up to  $L = 64$ , averaged over 1000 disorder realizations typically. In Sec. III B we discuss the local dynamic structure factor  $S_0(\omega)$ , i.e., the  $\mathbf{q}$  averaged  $S(\mathbf{q}, \omega)$ . In addition to results for  $p = 1/16$  and  $p = 1/8$ , we also consider the case of a single vacancy and compare with results for the clean system. In Sec. III D we show results for the real-space resolved spectral function  $S(\mathbf{r}, \omega)$  in different frequency windows (“tomography”), which allows us to formulate a more complete picture of the nature of the different types of excitations.

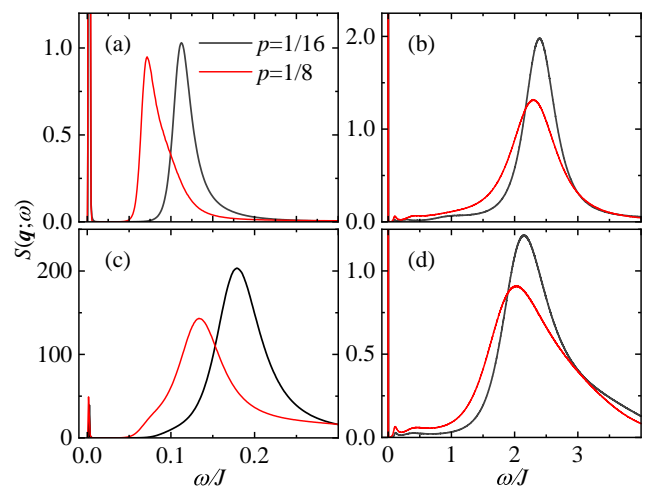


FIG. 7.  $S(\mathbf{q}, \omega)$  for  $L = 64$  at representative  $\mathbf{q}$  points for  $p = 1/16$  (black curves) and  $p = 1/8$  (red curves). The  $\mathbf{q}$  points are: (a)  $\mathbf{q} = (2\pi/L, 0)$ , (b)  $\mathbf{q} = (\pi/2, \pi/2)$ , (c)  $\mathbf{q} = (\pi - 2\pi/L, \pi - 2\pi/L)$ , (d)  $\mathbf{q} = (\pi, 0)$ . Note that the  $\omega$  scale is the same for the pairs (a), (c) and (b), (d).

#### A. Multiscale excitation structure and momentum dependence

For some initial observations, we show  $S(\mathbf{q}, \omega)$  for  $L = 64$  at four representative momenta in Fig. 7, comparing results for the two different vacancy fractions. In all cases, the rotor mode at very low frequency, discussed in the case of a small system in Sec. II D, is apparent, and there is a clear separation between this very narrow peak and the other features of the spectrum. The rotor peak is clearly much narrower than in Fig. 2, and we will show below that it systematically narrows with increasing system size while moving down toward  $\omega = 0$ .

At the momenta closest to  $\mathbf{q} = (0, 0)$  and  $(\pi, \pi)$ , shown in Fig. 7(a) and Fig. 7(c), respectively, there is an asymmetric main peak that moves down in frequency upon increasing  $p$  while also broadening somewhat. On the magnetic zone boundary, Fig. 7(b) and 7(d), the dominant peak is also slightly broader for the larger  $p$  value, though less so in relation to the peak energy. In addition to what is most naturally interpreted as a highly damped magnon peak with a substantial multimagnon tail (extending to  $\omega \approx 5J$  at the zone boundary), there is also a substantial almost flat portion at low energies, ending at a small peak that is clearly separated from the rotor peak. As we will show below, the peak corresponds to the localized mode discussed by Chernyshev et al. [15].

The localization peak should also be present in Figs. 7(a) and 7(c), but its relative contribution there is small and its location is within the left part of the visible peak. At these momenta, which correspond to long-wavelength uniform and staggered fluctuations, separating the expected different features of the spectrum above the low-energy rotor peak is not possible within the res-

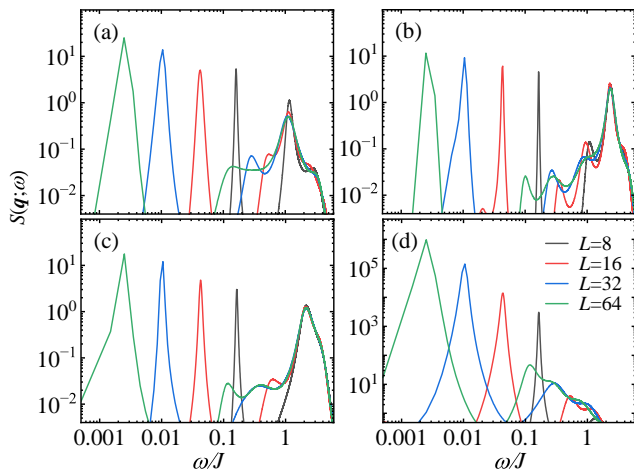


FIG. 8. Log-log plots of  $S(\mathbf{q}, \omega)$  for  $p = 1/16$  at (a)  $\mathbf{q} = (\pi/4, 0)$ , (b)  $\mathbf{q} = (\pi/2, \pi/2)$ , (c)  $\mathbf{q} = (\pi, 0)$ , (d)  $\mathbf{q} = (\pi, \pi)$ .

olution of our method. This state of affairs also likely reflects the expectation that all the features corresponding to localized excitations and propagating modes should merge close to  $\mathbf{q} = (0, 0)$  and  $(\pi, \pi)$ , reflecting fully incoherent quantum dynamics [15]. We will therefore mainly focus our investigations on points further away from these limits, where we can reliably separate different contributions of the multiscale spectral functions.

The very substantial broadening of the main peaks in Figs. 7(b) and 7(d), for  $\mathbf{q}$  close to the magnetic zone boundary, is absent in the  $T$ -matrix studies [9, 15], where the interactions between the magnons and the local impurity states were not accounted for. Some broadening was observed in an exact diagonalization study of the linear spin wave Hamiltonian with vacancies [16], but not to the extent that we find here. In particular, the long tail, which extends as far as to  $\omega/J \approx 5$ , beyond the  $\omega$  scale used in Figs. 7(b) and 7(d), is missing, which indicates that it arises from multimagnon excitations in the fully interacting system.

To study the size dependence, in Fig. 8 we graph results for  $p = 1/16$  in log-log plots so that the low energy features can be examined more clearly. Since the spectral functions are accumulated in histograms, at very low  $\omega$  scales the dominant spectral weight corresponds to only a small number of histogram bins, causing the peaks to appear less smooth. It is nevertheless apparent that the lowest peak moves down rapidly as  $L$  increases, exactly as would be expected for an Anderson quantum rotor mode of a system with long-range Néel order.

Considering the log scale for  $\omega$  in Fig. 8, the rotor peak also narrows with increasing  $L$ , reflecting less fluctuations in the lowest excitation (recall Fig. 2) as the magnitude of the Néel order stabilizes. For fixed system size the peak is located at the same energy at all momenta. As shown in Fig. 9, this energy scales with the system size in the expected way as  $1/N = 1/L^2$  for an Anderson quantum rotor state.

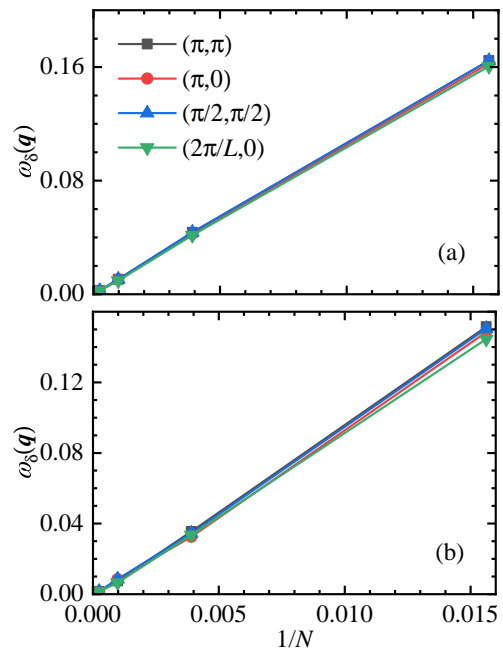


FIG. 9. Energy of the lowest-energy peak in  $S(\mathbf{q}, \omega)$  at four different momenta (from results such as those in Fig. 8) vs the inverse lattice volume  $1/N = 1/L^2$ . The dilution fraction is  $p = 1/16$  in (a) and  $p = 1/8$  in (b). The energy being the same at all momenta at fixed  $N$  and the asymptotic  $1/N$  scaling confirm the identification of the peak as the lowest Anderson quantum rotor excitation.

Returning to Fig. 8, the low-energy feature above the rotor peak also moves down in frequency with increasing system size, as shown in more detail on a linear scale for one  $\mathbf{q}$  point at  $p = 1/16$  Fig. 10. Here as well the size shift is roughly  $\propto 1/N$ , but we are not able to carry out a reliable extrapolation to infinite size. Within estimated uncertainties, the peak location extrapolates to zero, but most likely it tends to a very small non-zero  $\omega$  value.

The predicted energy scale associated with the localized mode is  $\omega_{\text{loc}} \propto \exp(-\pi/4p)$  [15], which at  $p = 1/16$  would indeed be too small to resolve using our  $S(\mathbf{q}, \omega)$  results for sizes up to  $L = 64$ . The separation to the rotor peak and the narrowing of the second peak with increasing system size nevertheless lend support to this feature reflecting a specific type of excitation different from the quantum rotor below and magnon above. The presence of the feature throughout the BZ at low energy with no detectable dispersion suggest that it indeed reflects the predicted localized excitations of large spatial extent. In further support of a dispersionless mode, in Sec. IIIB we will discuss a much sharper peak in the local ( $\mathbf{q}$  integrated) structure factor, allowing for  $L \rightarrow \infty$  extrapolation of the localization energy at  $p = 1/8$ .

Yet another important aspect of the results in Fig. 8 is that the broad high-energy features converge rapidly with increasing system size, while the low energy tail, with an edge eventually forming the localization peak, builds up gradually. This consistent evolution of the

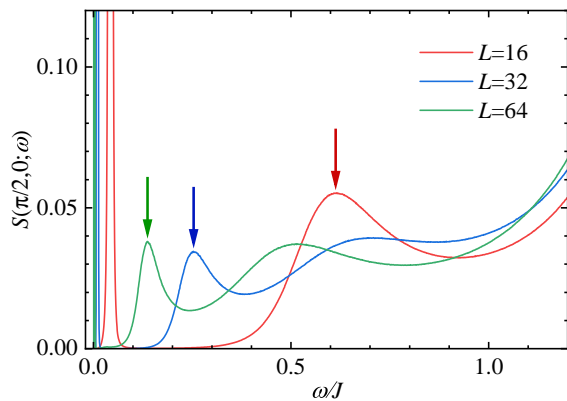


FIG. 10. Low-energy part of the dynamic structure factor at  $\mathbf{q} = (\pi/2, 0)$  and dilution fraction  $p = 1/16$ , shown for system sizes  $L = 16, 32$  and  $64$ . The position of the size dependent localization peak is marked by arrows.

spectral weight is natural in light of the exact form of the spectral function Eq. (4), where a higher density of  $\delta$  functions is expected with increasing  $L$ . An excitation associated with a large length scale will also be fundamentally limited by the inverse system length, leading to higher energy for smaller  $L$  (as we have seen quantitatively in the case of the quantum rotor state). Thus, the observed convergent high-energy features and evolving low-energy tail are consistent with expectations and unlikely artifacts of the analytic continuation procedures.

In Fig. 11 we compare  $p = 0, 1/16$ , and  $1/8$  results for  $S(\mathbf{q}, \omega)$  in our largest systems,  $L = 64$ . As in many plots in Ref. 15, we here focus on  $\mathbf{q}$  points on the diagonal  $(x, x)$  line of the BZ. In the case of  $p = 0$ , we also compare results of unrestricted SAC, discussed in Sec. IIC, and a constrained parametrization with a macroscopic  $\delta$  peak imposed at the lower edge in addition to the large number of “small”  $\delta$  functions representing the continuum above it (i.e., with the constraint that the continuum does not extend below the  $\delta$ -edge). The relative weight  $A_0$  of the macroscopic  $\delta$  function is fixed in the SAC process while its location is also sampled (though it fluctuates very little after the sampling has equilibrated). A scan over  $A_0$  reveals its optimal amplitude as quantified by  $\langle \chi^2 \rangle$ . For technical details of SAC with the  $\delta$ -edge parametrization we refer to Refs. 32 and 36.

At  $p = 0$ , the  $\delta$ -edge parametrization separates the expected sharp magnon peak and the multi-magnon continuum, which is not possible with the broadening effects of the unrestricted SAC, though the peak locations are nevertheless almost the same. The broadening of the sharp peak with unrestricted sampling reflects the  $\omega$  dependent resolution (better for smaller  $\omega$ ) imposed by the statistical errors of the QMC data. The reason for the better resolution at lower energy is simply because the contributions from such features remain statistically significant up to larger imaginary times, i.e., there is more information on low-energy features in the available  $G(\mathbf{q}, \tau)$  data.

The broadened peaks in Fig. 11(a) are also somewhat

asymmetric, reflecting the continuum above the magnon peak that cannot always be well resolved as a separate part of the spectrum unless the  $\delta$ -edge is imposed. A small secondary maximum is still also present and often close in shape to what is obtained with the  $\delta$  edge constraint, as seen in the insets of Fig. 11(a). The secondary peak or broad feature is most naturally interpreted as a multimagnon continuum [37]. For  $\mathbf{q}$  in the neighborhood of  $(\pi, 0)$ , the main magnon peak is greatly diminished and the continuum is more prominent, which is interpreted as a precursor to spinon deconfinement [35, 36].

For  $p > 0$ , in Figs. 11(b) and 11(c) the dominant peaks are much broader than the resolution limited magnons in Fig. 11(a) obtained with unrestricted SAC. Thus, at least the high-energy features should not be affected by the resolution of the method, given also that the QMC data quality is similar for all  $p$  values. The ability of our method to accurately resolve both high-energy and low-energy features is also supported by the tests in Fig. 2, though in that small system there is no structure between the rotor peak and the rest of the spectrum—there are also no spurious features, a fact which also can be taken as support for the emergent features for the larger system being correct.

In all cases, we also observe the extremely sharp peak at the lowest frequency, which we again associate with the quantum rotor excitation discussed previously. In Fig. 11 its  $\propto 1/N$  energy is practically zero on the scale used ( $\approx 0.002$  according to Fig. 8). As already discussed, but seen more clearly in the  $p = 1/8$  results in Fig. 11(c), in particular, spectral weight below the large broad peak extends to very low energy, with a gap remaining to the rotor peak. We can identify the localization peak using the interpretation of Ref. 15. We now discuss the features above this peak, starting from high energy.

For all momenta in Figs. 11(b) and 11(c), the main peak is shifted to lower frequency relative to the  $p = 0$  magnon, with the relative shift larger for smaller  $g$ . The dispersion relations for  $p = 1/16$  and  $p = 1/8$  along a cut in the BZ are graphed in Fig. 12. Here we define the excitation energy at  $p > 0$  based on the peak maximum, while at  $p = 0$  it is the location of the  $\delta$  function edge shown in Fig. 11(a). Similar  $p = 0$  results were obtained in Ref. [36], but there only up to  $L = 48$ . The size dependence at the  $\mathbf{q}$  points available for given  $L$  is rather weak except at  $(\pi, \pi)$ , as also seen in Fig. 12.

Despite the substantial broadening of the peaks for  $p > 0$ , the energy at and around the zone boundary is very close to that of the magnon at  $p = 0$ . It is particularly noteworthy that even the characteristic dip in energy at  $\mathbf{q} = (\pi, 0)$  of the clean system [33, 34] remains at vacancy fraction as high as  $p = 1/8$ . This dip can be related to locally correlated resonating singlets and was shown to be a precursor to the deconfined quantum phase transition into a non-magnetic valence-bond solid state in an extended parameter space [36]. The dip is magnified when an interaction bringing the system closer to the phase transition is added, as we will also find here for the



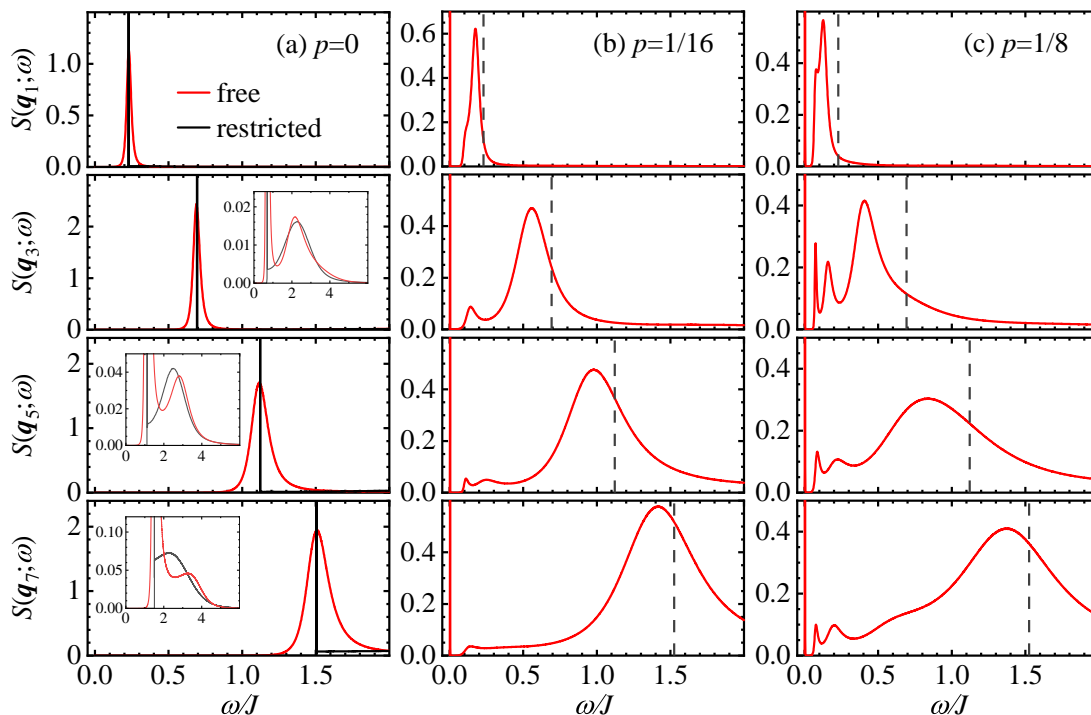


FIG. 11.  $L = 64$  results for  $S(\mathbf{q}, \omega)$  with  $\mathbf{q}$  on a diagonal of the BZ,  $\mathbf{q}_x = 2\pi(x, x)/L$ ,  $x = 1, 3, 5, 7$ . Results for a pristine system ( $p = 0$ ) are shown in (a), while (b) and (c) are for  $p = 1/16$  and  $p = 1/8$ , respectively. The red curves show results of unconstrained SAC sampling, while the black curves in (a) include a macroscopic  $\delta$  function (modeling a sharp quasi-particle peak) with optimized weight and continuum only above the peak. The resulting multimagnon continua are shown in more detail in the insets. The location of the peak in (a) is indicated by the dashed lines in (b) and (c). Note that the rotor peak is very close to  $\omega = 0$  (as is clearer from the  $L = 64$  results in Fig. 8); a small range of negative values are included on the  $\omega$  axis to make this sharp peak better visible.

diluted systems in Sec. V. The presence of the “spinon precursor” also for the diluted system is another indication that the high-energy excitation can still be characterized as a magnon, with significant damping and more multimagnon contributions to  $S(\mathbf{q}, \omega)$  than in the clean system.

Naively, the robust high-energy excitation reflects uniformity of the system on length scales less than the typical separation between vacancies. The broadening reflects the substantial damping effects of the disordered environment surrounding the uniform patches. When the energy drops well below the  $p = 0$  magnon, the peak also narrows significantly, as seen in in Figs. 11(b) and 11(c), while a long thin high-energy tail still remains. A broadening of order  $pk$  (with  $k$  the momentum relative to either of the two low-energy points) was predicted [15], and in Figs. 11(b) and 11(c) we indeed also observe systematically reduced broadening as  $q$  approaches 0, though the proportionality to  $p$  is not apparent in all cases.

The significant drop in magnon energy close to  $\mathbf{q} = (0, 0)$  and  $(\pi, \pi)$  is further highlighted by Fig. 13, where the dispersion relations are shown relative to the linear spin wave energy  $\omega_0(\mathbf{q})$  of the clean system. Here we also show the predicted anomalous dispersion relation

$$\omega_{\text{ano}}(k) = ck[1 - p(\pi/2 - 1) + \ln(ck/4)/\pi], \quad (14)$$

which is Eq. (51) from Ref. 15 with the limit  $k \rightarrow 0$  taken but the full  $p$  dependence is kept—in Eq. (1) the limit  $p \rightarrow 0$  was also taken. However, the expression is still only expected to be valid for small  $p$  and then the further simplified form in Eq. (14) is also very similar.

Our results for  $p = 1/16$  in Fig. 13(a) indeed match the predicted form slightly better than those for  $p = 1/8$  in Fig. 13(b). To optimize the fits, we adapted the spin wave velocity for both  $p = 1/16$  and  $p = 1/8$ . The optimal values, listed in the caption of Fig. 13, are marginally larger than the linear spin-wave value  $c_0 = \sqrt{2}J$  but smaller than the estimate  $c \approx 1.63$  for  $p = 0$  (renormalization factor 1.16) [36, 53]. The smaller velocities for  $p > 0$  are natural in light of the smaller mean couplings, though it is difficult to judge exactly what the optimal  $c$  values are, given that the agreement with the theory is never perfect. The agreement is in general slightly better near  $(\pi, \pi)$  than near  $(0, 0)$ .

The predicted form should be valid only for  $\mathbf{q}$  in the neighborhood of  $(0, 0)$  and  $(\pi, \pi)$  and must also eventually break down very close to these points, reflecting the incoherent dynamics at the lowest energies where the magnon should merge with the localized excitations. We have also tried to fit our results to the full form Eq. (51) of Ref. 15, which avoids the continued increase above the

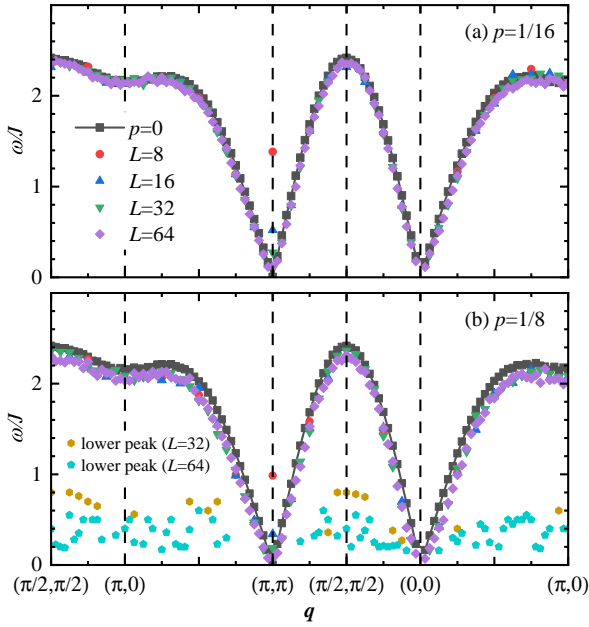


FIG. 12. Dispersion relations along a cut through the BZ. The magnon peak location for system sizes  $L = 8, 16, 32,$  and  $64$  is shown for  $p = 1/16$  in (a) and  $p = 1/8$  in (b). Results for the clean  $L = 64$  Heisenberg model is shown as a reference in both cases. In (b), the location of the peak below the magnon (the proposed random network excitation) is shown for  $L = 32$  and  $64$  at momenta where the feature is clearly discernible in results such as those in Fig. 11.

baseline spin wave dispersion seen in Fig. 13. However, the agreement with our data around  $\mathbf{q} = (0, 0)$  and  $(\pi, \pi)$  is not further improved and the zone boundary energy cannot be matched well (it is too low) when  $c$  is adapted to the anomalous dispersion; we do not show graphs here.

The reasonable good match between the anomalous magnon dispersion and our numerics over a substantial part of the BZ provide strong support for the validity of both approaches. However, the peak present in between the localization and magnon peaks, most clearly visible in 11(c), was not predicted by the  $T$ -matrix theory. As already mentioned in Sec. IB, we believe that this peak reflects another propagating excitation arising from randomly located effective moments adjacent to vacancies. While we have not explicitly constructed an effective model of the subsystem making up the random network, which would require knowledge of the interactions mediated by the bulk medium, the participating spins can be clearly observed in the real-space dynamic structure factor  $S(\mathbf{r}, \omega)$  in the relevant energy window, as will be shown below in Sec. III D.

In Figs. 12(b) and Figs. 13(b) we have also included the location of the energy of the proposed random network mode at  $p = 1/8$ , where the peak is larger and appears more consistently in our results than at  $p = 1/16$ . Because of the very significant scatter, it is not possible to make any strong statements about the dispersion rela-

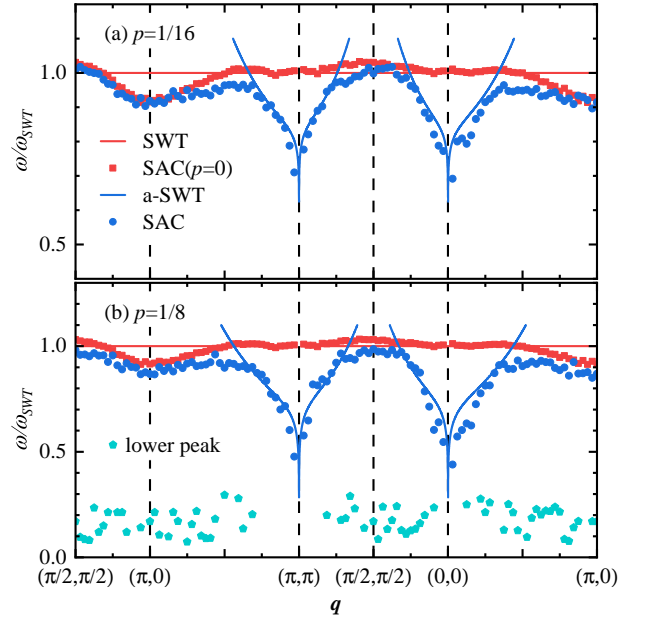


FIG. 13. The  $L = 64$  peak energies from Fig. 12 shown relative to the dispersion relation  $\omega_0(\mathbf{q})$  in linear spin wave theory (including the estimated spin-wave velocity renormalization factor 1.16 [36, 53]). The magnon energies at  $p = 0$  and  $p > 0$  are shown with red squares and blue circles, respectively, and the lower energy of the proposed random network mode is shown with the teal hexagons. The blue curves show the predicted anomalous dispersion relation Eq. (14), where in (a) and (b) we have set the spin wave velocity to  $c = 1.58$  and  $c = 1.54$ , respectively, i.e., the renormalization factor  $c/c_0 = c/\sqrt{2} \approx 1.12$  in (a) and  $1.09$  in (b), smaller than  $c/c_0 \approx 1.16$  at  $p = 0$ .

tion, however. There is also some visible size dependence, as is apparent for  $L = 32$  and  $64$  in Fig. 12(b).

As seen more clearly in Fig. 13(b), the results are less noisy close to  $\mathbf{q} = (0, 0)$  and appear to show an increasing trend for small  $q$ . We lack reliable data close to  $\mathbf{q} = (\pi, \pi)$ , but the existing points are at least also consistent with a maximum there as well. Given that these are results relative to the linear spin wave dispersion, the upturn may possibly indicate that the dispersion of the random network excitation is effectively sublinear before it and the main magnon peak merge with the localized excitations at low energy.

It should be noted that, the number of disorder realizations used here (1000) is not sufficient to make the vacancy distribution at  $p = 1/16$  very uniform on average, and the density fluctuations also translate to momentum space. The fact that the localization peak and low-energy spin wave peak are clearly observed at some momenta but not at others, as exemplified by the results in Fig. 11(b), is therefore not necessarily a reflection of limited frequency resolution of the SAC method, but may very well be the true behavior of  $S(\mathbf{q}, \omega)$  averaged over the finite set of vacancy realizations used. For  $p = 1/8$  the mean vacancy distribution is naturally more

uniform, and we can extract the energy of the random network mode more reliably, though still with significant statistical fluctuations.

In the  $T$ -matrix theory, disorder averaging is carried out at the level of the Green's function before it is used to generate the spectral function. No structure in  $S(\mathbf{q}, \omega)$  was generated between the localization and magnon peaks, in contrast to the intermediate peak observed here. In Sec. III D we will demonstrate that the localized excitations are associated with a very small number of spins at vacancies. Such specific sparse local degrees of freedom may not be reflected when using the disorder averaged Green's function, and it is then possible that the localized mode in the analytic theory [15] is not exactly of the same nature as in the fully interacting spin model. The extrapolated localization energy at  $p = 1/8$ , which we obtain below in Sec. III B from the local dynamic structure factor, is in fact much higher than the predicted value.

Another discrepancy between our results and the theory is that a double-peaked  $S(\mathbf{q}, \omega)$  forms in the latter when the magnon resonates with local impurity states at energy of order  $J$  [9, 15]. The interactions are not fully taken into account by the  $T$ -matrix approach, and the zone boundary magnons therefore appear essentially as a band of excitations separated from those with the anomalous dispersion at lower energy. A broad peak with two different, not far separated maximums is consistently seen in the numerical spin wave calculations in Ref. [16], even beyond the  $\mathbf{q}$  range where it appears in the  $T$ -matrix calculations. We always find just a single peak, which suggests that, indeed, neglected interactions cause an artificial feature in the spin wave calculation of the spectral function. Regardless of the interpretation, we now also have an unbiased quantitative characterization of the high-energy part of  $S(\mathbf{q}, \omega)$ , which was an open issue previously [15].

## B. Local dynamic structure factor

Here we examine the local dynamic structure factor  $S_0(\omega)$ , where the operator in Eq. (4) is  $O = S_{\mathbf{r}}^z$  and we take the average over all lattice points  $\mathbf{r}$ . This quantity also is equivalent to  $S(\mathbf{q}, \omega)$  averaged over all  $\mathbf{q}$ , a fact which represents another opportunity to test the SAC approach: We can either run the SAC for all momenta separately and then average the resulting spectra over  $\mathbf{q}$ , or we can average  $G(\mathbf{q}, \tau)$  over  $\mathbf{q}$  first, resulting in  $G_0(\tau)$  (where now the subscript 0 refers to the distance-0 case, i.e., the on-site correlation function), which can be computed directly in real space (averaged over locations) and analytically continued for  $S_0(\omega)$ . The two different ways of computing  $S_0(\omega)$  should in principle be equivalent, but in practice, because of the noisy imaginary-time data and imperfections of the analytic continuation, the results will differ to some extent, thus providing some measure of the reliability of the SAC approach. This kind

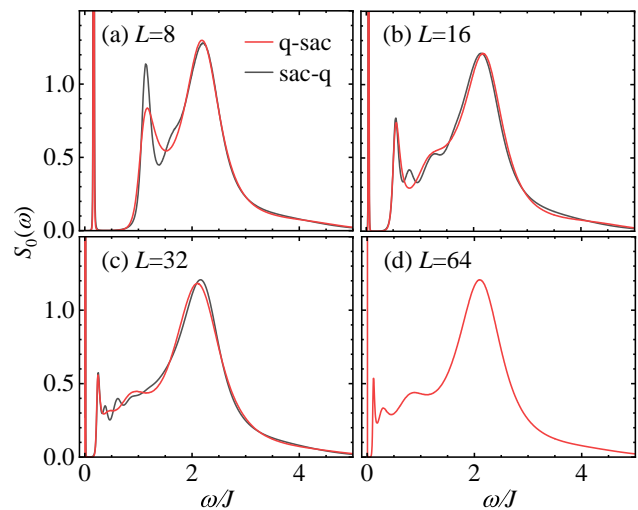


FIG. 14. Local spectral function averaged over sites and disorder realizations at  $p = 1/16$  for system sizes (a)  $L = 8$ , (b)  $L = 16$ , (c)  $L = 32$ , and (d)  $L = 64$ . The red curves correspond to momentum summation before analytic continuation, i.e., applying SAC to the local correlation function  $G_0(\tau)$  averaged over all spins, while the black curves were obtained by applying SAC to all  $G(\mathbf{q}, \tau)$  and averaging after.

of test was previously applied with the MEM to study the local dynamic response of the Heisenberg chain [54], and also with the SAC method in the case of the random Heisenberg chain [55].

Figure 14 shows  $p = 1/16$  results for system sizes  $L = 8, 16, 32$ , and  $64$ . For the largest system we did not compute  $G(\mathbf{q}, \tau)$  for all  $\mathbf{q}$  (only on high-symmetry lines for which results were presented in Sec. III A). For the other systems, the results of the two calculations agree very well on the location and width of the quantum rotor peak, the low-energy edge and peak above it, and also in the entire frequency range of the main peak. For  $L = 16$  and  $32$ , the results from averaging  $S(\mathbf{q}, \omega)$  exhibit wiggles that are likely finite-size effects resulting from the peaks in the individual  $\mathbf{q}$  spectra, which are not sufficiently dense on the  $\mathbf{q}$  grid for small  $L$  (as was also found for the random Heisenberg chain in Ref. 55). It is not realistic to expect SAC applied to  $G_0(\tau)$  to resolve these fine structures—to the extent that they are even completely reliable in the location and width of the small peaks. Since such oscillations would not be expected in the thermodynamic limit, not resolving them may in a sense correspond to faster convergence with  $L$ .

From now on we discuss only the method of applying SAC to  $G_0(\tau)$ ; the red curves in Fig. 14. It is interesting to see that more structure gradually develops above the quantum rotor peak as  $L$  increases. For  $L = 8$ , there are just two broadened peaks above the already well isolated and narrow rotor peak, while for  $L = 16$  there is a hint of a third intermediate peak forming, which is more completely developed for  $L = 32$  and further grows in size for  $L = 64$ . For  $L = 64$  there is another peak above the

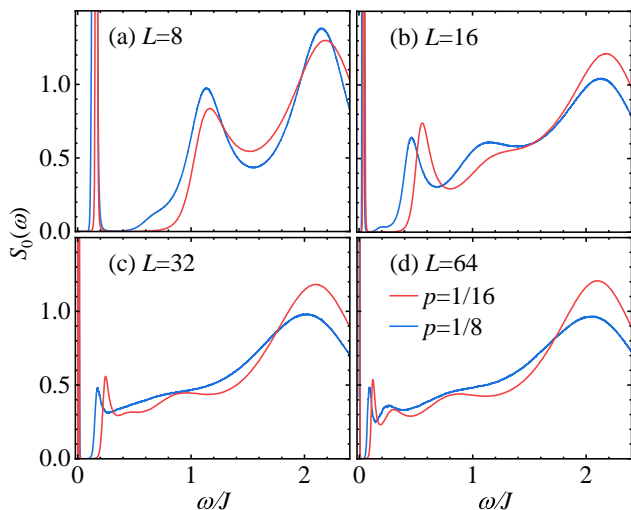


FIG. 15. Local spectral function obtained from the site averaged  $G_0(\omega)$  at  $p = 1/8$  (blue) and  $p = 1/16$  (red) for system sizes (a)  $L = 8$ , (b)  $L = 16$ , (c)  $L = 32$ , and (d)  $L = 64$ .

edge, of which some hints are already seen at  $L = 32$ .

The four peaks that are clearly formed for  $L = 64$  above the obvious rotor peak can all be understood based on the picture of the excitations developed in Sec. III A. The peak at the low-energy edge is clearly the localization mode. It becomes sharper and diminishes in relative weight as  $L$  increases—a rough extrapolation shows that the peak height remains finite as  $L \rightarrow \infty$ . The energy scale of the second peak is consistent with the  $\mathbf{q}$  averaged random network excitations, as is apparent by comparing with Fig. 12(b), despite the large scatter in the location of the lower peak and  $p = 1/8$  in that figure (we will see below that the location of the peak is not much different for  $p = 1/8$ ). The remaining features are then due to the magnon, with the small bump on the left side of the main broad peak consistent in its energy scale with contributions from  $\mathbf{q}$  close to  $(0, 0)$  and  $(\pi, \pi)$ , where a large drop in energy compared to the  $p = 0$  dispersion is seen in Fig. 13. The narrowing of the peak seen at the smaller  $q$  values in Fig. 11(b) is also required for the formation of a separate peak from these spin waves in the momentum regime where their energies are strongly reduced.

Figure 15 shows similar results at vacancy fraction  $p = 1/8$ , only for the case of analytical continuation of the local function  $G_0(\tau)$ . We also include the  $p = 1/16$  results from Fig. 14 in order to compare the two cases. At  $p = 1/8$  the four features of the spectrum emerge slower as  $L$  increases, which can be understood as due to further broadening of the main high-energy peak. Nevertheless, for  $L = 64$  we observe all the same features qualitatively at both  $p$  values. In particular, the first sharp peak above the rotor peak is consistent with the localization peak or edge seen at very similar energy in Figs. 11(b) and 11(c), and the second peak is consistent with the overall energy scale of the random network mode according to the results in Fig. 12(b).

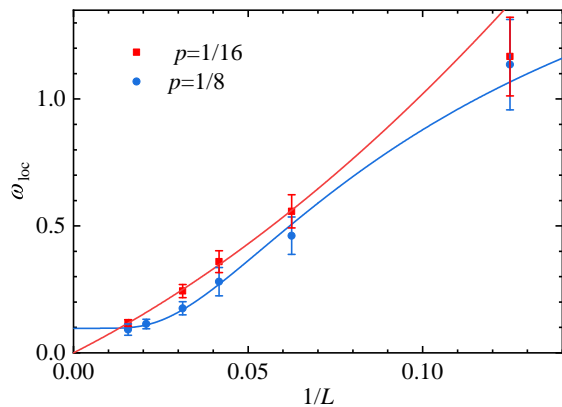


FIG. 16. Inverse system size dependence of localization energies determined using  $S_0(\omega)$  data such as those in Fig. 15 at  $p = 1/16$  (red squares) and  $p = 1/8$  (blue circles). The error bars correspond to half of the width at the half maximum on the left side of the  $S_0(\omega)$  peaks. The fitted curve for  $p = 1/8$  is of the form  $\omega_{\text{loc}} = a + be^{-cL}$  with free parameters  $a, b, c$  and including all system sizes. For  $p = 1/16$  a fit of the form  $a/L + b/L^2$  is shown only as an illustration of non-asymptotic behavior, with the asymptotic gap too small to determine.

The localization peak in  $S_0(\omega)$  is much sharper than the corresponding momentum resolved peaks, e.g., in Figs. 11(b) and 11(c). We have extracted the peak locations for the system sizes used above, and also for  $L = 24$  and 48. It is difficult to establish an absolute statistical error on the peak location, and instead we use the half width at the half maximum on the left side of the  $S_0(\omega)$  peaks as an estimate of the uncertainty of the finite-size localization energy. The results for both dilution fractions are graphed versus  $1/L$  in Fig. 16.

We should expect the localization energy to increase with  $p$  [15], but for each individual size the  $p = 1/16$  energy is actually above that for  $p = 1/8$ , as also seen in Fig. 15. However, the results for  $p = 1/8$  indicate a flattening-out for the larger sizes, suggesting an eventual swapping of the order of the peaks for larger  $L$ . Given that the localized excitations should have a typical size, an exponential convergence of the energy  $\omega_{\text{loc}}(L)$  versus the system size should be expected asymptotically for sufficiently large  $L$ . For  $p = 1/8$ , the observed flattening of the data for the largest system sizes in Fig. 16 clearly demonstrates a non-zero energy in the thermodynamic limit, and an exponential form fits the data well from the smallest to the largest system size ( $8 \leq L \leq 64$ ). This fit extrapolates to  $\omega_{\text{loc}} = 0.10 \pm 0.01$ , which is about 50 times larger than the predicted [15] order of magnitude of the localization energy,  $e^{-\pi/4p} \approx 0.0019$ . However, the prefactor of the exponential was not determined, and the form may also only apply to much smaller dilution fractions.

For  $p = 1/16$ , the results in Fig. 16 do not show any tendency to an exponential flattening out, suggesting that the system sizes  $L \leq 64$  are still much smaller than the typical localization length. Fitting to a second-order



polynomial for the  $L \geq 16$  data, the extrapolated energy is slightly negative but also consistent with a small positive value. For the fit shown in Fig. 16, we have set the constant to zero. This fit is just to illustrate the fact that the actual localization energy is too small to determine based on the available system sizes, which would be a natural conclusion also under the assumption that  $\omega_{\text{loc}} = Ae^{-\pi/4p}$  with  $A \approx 50$  from the result for  $p = 1/8$ , which would imply  $\omega_{\text{loc}} \approx 0.0002$  for  $p = 1/16$ .

It should be noted that the sharp localization peak in  $S_0(\omega)$  does not necessarily imply that the system is gapped. In fact, the low-energy tail of the peak should be expected to extend down to  $\omega = 0$  in the thermodynamic limit, reflecting the existence of arbitrarily large local excitations despite there being a typical size (predicted to be of the order  $e^{\pi/4p}$  [15]). The probability of excitations larger than the typical scale will be exponentially small, and the spectral tail should then be exponentially thin for  $\omega \rightarrow 0$ . Many thermodynamic quantities at  $T < \omega_{\text{loc}}$  will in practice appear to show a gap.

### C. Single vacancy

It is also useful to examine the local spectral function in the case of a single vacancy, which we show in Fig. 17 for several distances close to the vacancy along with results for the clean system. The significant quantum rotor peak is seen clearly in all cases. All the spectra look rather similar, except at the sites closest to the vacancy,  $r = 1$ , where we observe a large shift of the dominant peak to lower  $\omega$  and also a less sharp peak at lower energy. In all other cases, we find a sharp peak at  $\omega \approx 0.5$ —it is the tallest at  $r = 2$ , significantly suppressed at  $r = 3$ , and gradually approaches the height in the clean system.

In linear spin wave theory, the density of states for the clean system exhibits a van Hove like singularity at the band edge, due to the degeneracy of all states on the magnetic zone boundary. This degeneracy is broken for the true magnon, as seen here in Fig. 13. Moreover, there is a substantial continuum above the main magnon peak. Thus, the singularity in the density of states should be replaced by a broad peak, resulting in the high-energy profile seen in Fig. 17 for both the clean system and the single vacancy. The sharp peaks at  $\omega \approx 0.5$  are caused by the large matrix elements at momenta close to  $(\pi, \pi)$ , which are not included in the density of states calculated for both the clean system and the single vacancy, e.g., in Ref. 8. The impurity feature found there in the density of states at distance  $r = 1$  can still be roughly identified with the shifted main peak in Fig. 17.

Overall, comparing  $S_0(\omega)$  for a single vacancy with the profiles at  $p = 1/16$  and  $1/8$  in Fig. 15, the low energy features bear little resemblance. The high-energy features are similar, but with more weight in the tail above  $\omega \approx 4$  at  $p > 0$ . The static spin structure around a vacancy was previously studied with QMC simulations [25]. It corresponds to the frequency integrated local structure

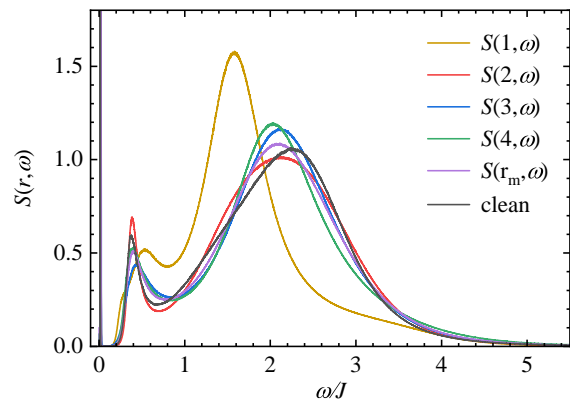


FIG. 17. Local spectral function at several short distances away from a single vacancy in a system of size  $L = 32$ . The numbers  $n = 1, 2, 3, 4$  in the legends indicate the  $n$ th closest neighbor of the vacancy, with  $r_m$  the farthest separation on the  $L = 32$  lattice. The result for the clean system is also shown for comparison.

factor in Fig. 17 and does not provide detailed information about the excitations.

### D. Real-space tomographic imaging

To gain insights into the spatial distribution of the different types of excitations at  $p > 0$ , we here study the real-space resolved spectral function  $S(\mathbf{r}, \omega)$  for individual vacancy realizations. In a tomographic procedure, we compute integrals over energy windows

$$D_k(\mathbf{r}) = \frac{N(1-p) \int_{a_k}^{b_k} S(\mathbf{r}, \omega) d\omega}{\sum_{\mathbf{r}} \int_{a_k}^{b_k} S(\mathbf{r}, \omega) d\omega}. \quad (15)$$

This function represent the relative participation of each individual spin in all the excitations with energy within the chosen windows  $[a_k, b_k]$ . We have normalized the weight distribution in Eq. (15) so that  $D_k(\mathbf{r})$  on average equals 1 on the sites with spins.

From a real-space map we can also construct a participation ratio, defined as

$$R_k = \frac{1}{N(1-p)} \frac{(\sum_{\mathbf{r}} D_k(\mathbf{r}))^2}{\sum_{\mathbf{r}} D_k^2(\mathbf{r})}, \quad (16)$$

where we have also normalized by the number of spins. Then  $R_k = 1$  if the spectral weight is evenly distributed on all spins, and, in the opposite extreme,  $R_k = 1/N(1-p)$  if all the weight is concentrated in on a single spin. A similar inverse participation ratio  $1/R$  was computed versus  $\omega$  in the real-space spin wave diagonalization study in Ref. 16 and also in the 2D Heisenberg model at the percolation point [28], in the latter case not using an energy window but the local susceptibility defined in Eq. (13).

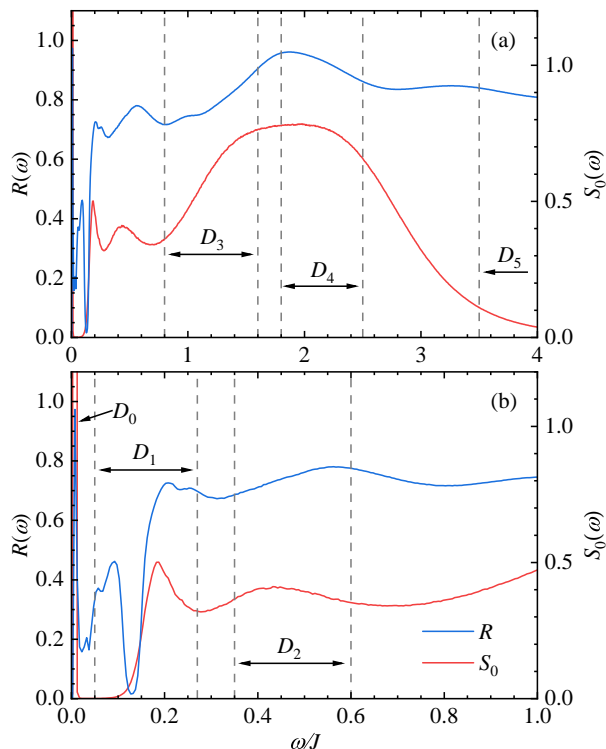


FIG. 18. Local spectral function (red curves) and participation ratio (blue curves) for an individual  $L = 32$ ,  $p = 1/8$  vacancy realization. The results are shown on different energy scales in (a) and (b). The frequency windows used to compute the integrals  $D_k$  (shown in Fig. 19, where the vacancy locations can also be seen) are also indicated.

Here we will use a large number of thin energy window for a function  $R(\omega)$  of an essentially continuous  $\omega$ , while maps  $D_k(\mathbf{r})$  will be shown for a few larger windows with  $\omega \in [a_k, b_k]$ , which for given “slice”  $k$  is selected so that it is dominated by one of the excitation types discussed previously. The selection of appropriate windows is aided by the  $\mathbf{r}$  average  $S_0(\omega)$  of  $S(\mathbf{r}, \omega)$ , which, for a sufficiently large system, we expect to contain similar structure as the disorder averaged local dynamic structure factor graphed in Fig. 15. The participation ratio also will be useful in this regard, as we will see. We here consider a single  $L = 32$  vacancy realization at  $p = 1/8$  and present similar results for  $p = 1/16$  in Appendix B.

### 1. Participation ratio

Figure 18 shows both the average dynamic structure factor  $S_0(\omega)$  and the participation ratio  $R(\omega)$ , with 18(a) showing almost the full energy range  $\omega \in [0, 4]$  and 18(b) focusing on details in the low-energy part. The spectrum for this single sample has a peak structure similar to the disorder average in Fig. 15, though with differences in details as expected.

The participation ratio shows an interesting structure,

being close to 1 in the very narrow energy range corresponding to the rotor peak, reflecting the fact that most of the spins participate in this excitation. On the left side of the localization peak in  $S_0(\omega)$ , there is a very low minimum in  $R(\omega)$ , showing that there is a narrow energy range where only a few spins are excited. The peak structure in  $R(\omega)$  between the rotor peak and the global minimum may not have much significance because the spectral weight there is very small. Moving further into the localization peak,  $R(\omega)$  grows sharply, then decreases somewhat before increasing slowly in the  $\omega$  region where the spectral weight of the low-energy propagating mode is concentrated. At higher energy still, a maximum forms within the energy range corresponding to the magnons, after which the behavior is rather flat (mildly decreasing) all the way to the far end of the tail of the spectrum.

Comparing the participation ratio  $R$  with  $1/R$  computed in the numerical spin wave calculation, the closest case to our  $p = 1/8$  is  $p = p_c/2 \approx 0.2$  in Fig. 4(b) of Ref. 16, where  $L = 36$ . Here also there is a tendency to a sharp drop in  $R$  at a low energy scale compatible with the localization scale that we find here. However,  $S(\mathbf{q}, \omega)$  at  $\mathbf{q} = (0.4\pi, 0)$ , graphed for an  $L = 32$  system in Fig. 8 of Ref. 16, does not show any signs of a localization peak at any  $p$ . There is also no peak corresponding to our random network mode.

### 2. Tomographic maps

Based on the results for both  $S_0(\omega)$  and  $R(\omega)$ , we have selected energy windows  $k = 0, \dots, 5$ , for constructing color coded real space maps  $D_k(\mathbf{r})$ . These windows are also indicated in Fig. 18, and the resulting maps  $D_1, \dots, D_4$  are shown in Fig. 19. We will discuss the map  $D_0$  of the rotor state in Sec. IV, and the high-energy window  $D_5$ , which we believe contains mainly multimagnon excitations, is discussed in Appendix B.

It should be kept in mind that the tomographic maps include all the excitations within the chosen window, and so informs us about the spins involved in forming an entire band of excitations, not individual excitations. The maps are not very sensitive to exactly how the energy windows are selected, as long as they each correspond to a region dominated by one of the excitations. Clearly these regions cannot be completely separated from each other, except that of the rotor map  $D_0$ , because all excitation modes are subject to broadening and we do not resolve the momentum structure here. Nevertheless, we will see that reasonably clear pictures of the different excitations emerge from the tomographic approach.

The map  $D_1$  should correspond to the localized mode, while  $D_2$  should roughly capture the low-energy propagating mode, which we here will argue arises from a random spin network. The maps  $D_3$  and  $D_4$  both cover the magnons, with the subdivision chosen so as to separate the contributions from the part of the BZ where the energy is close to  $\omega(\mathbf{q})$  of the clean system (Fig. 13),

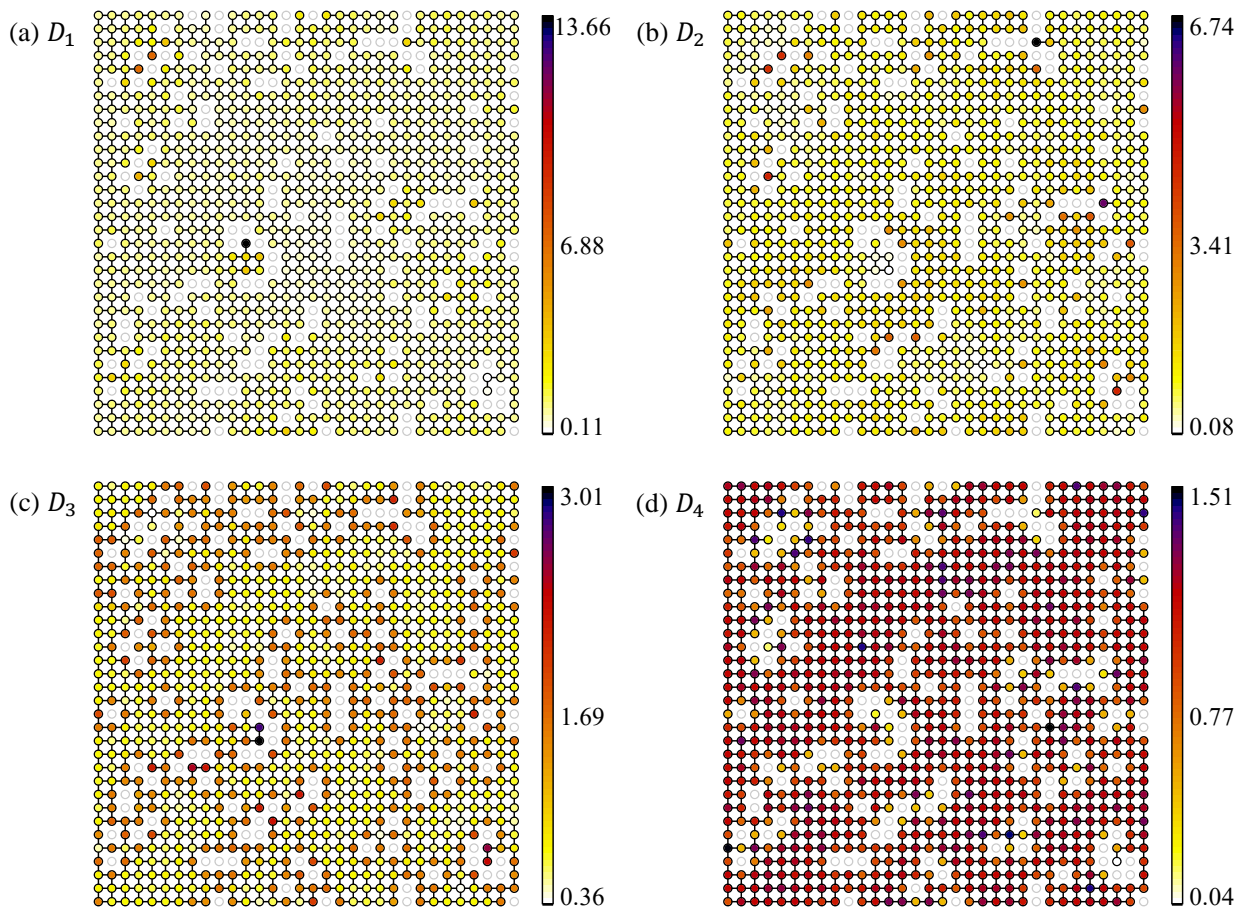


FIG. 19. Tomographic maps  $D_1$ - $D_4$  defined in Eq. (15) for an  $L = 32$  system at  $p = 1/8$ . The frequency windows are shown in Fig. 18 and the color maps correspond to the highest to lowest spectral weight for each case, as indicated. The dim circles represent vacancies. The mean spectral weight on the spins in all maps is unity.

in  $D_4$ , and when the dispersion is anomalous, in  $D_3$ . It should be noted that the low-energy magnons will also to some extent reach down to the random network excitations, since they are both damped modes and merge together somewhere close to the localization energy.

The weight  $D_1(\mathbf{r})$  of the localized excitations, shown in Fig. 19(a), is concentrated on a rather small number of sites adjacent to the vacancies (i.e., those with less than four nearest neighbors), which explains the small participation ratio in most of this window. Almost all of the sites with large weight belong to monomer rich regions—the results of the dimer-monomer simulation of this system are presented in Appendix B. Thus, it appears that the localized states are formed primarily by spins in regions of local sublattice imbalance.

Another interesting aspect of the spins with large spectral weight in  $D_1$  is that most of them have only one neighbor, as seen in Fig. 19(a). We have also computed separately the relative spectral weight on the spins with a single neighbor, finding a very sharp peak at the energy where the participation ratio is very small in Fig. 18. This behavior is another indication of the localized states

being qualitatively different from the states immediately above them.

Moving to  $D_2$  in Fig. 19(b), a large fraction of the spectral weight here is distributed on a subset of the spins next to vacancies—but many more spins than in  $D_1$  and most of them not belonging to monomer rich regions. Note also that some spins that have very little spectral weight in  $D_2$  have much larger weight in the localization map  $D_1$ , and vice versa.

The  $D_2$  map is what motivates our proposal of the random network mode. Most likely the subsystem strongly involved in these excitations consists predominantly of those spins that are effectively the least coupled to the bulk Néel order, because of a small number of neighbors but also subtle details of their environment. These more easily excitable spins should be coupled to each other through an effective interaction mediated by the bulk degrees of freedom, which naturally leads to an energy scale below the bare Heisenberg coupling  $J$ .

Qualitatively, the picture of the random network mode is similar to that of the localized excitations at still lower energy, but in that case the number of spins involved

is much smaller and there is a strong overlap with the regions of classical monomers. An interesting question, the full answer to which is beyond the scope of the present work, is whether an effective random network model of  $S = 1/2$  spins would be able to explain also the localized states, i.e., whether such a model can host both localized and propagating excitations of the nature found here. Since the full diluted Heisenberg model is capable of this, there is no obvious reason to expect the contrary for an effective model including only spins at vacancies, with suitable interactions. Most likely, coupling of the spins to the global Néel order also has to be taken into account by an external staggered field.

As mentioned, the  $D_2$  window should also be to some extent influenced by the low-energy magnons, and it is possible that the weak, almost uniform background spectral weight in this map arises primarily from the magnons. Thus, the actual random network excitation may be even more concentrated on the subset of spins with large  $D_2$  spectral weight, which would strengthen the case for an effective model involving only spins next to vacancies. Shifting the  $D_2$  window to lower energy, to reduce the influence of the magnons, indeed leads to less weight on the patches between vacancies. This behavior is also clear from the behavior of  $R(\omega)$  in Fig. 18(b) for  $\omega \in [0.3, 0.6]$ , where  $R$  decreases (less spins participate) as the energy is lowered.

Before discussing the weight  $D_3$  in the following window, it is more instructive to first look at  $D_4$ , from the window in Fig. 15 covering the upper end of the main peak in  $S_0(\omega)$  and also the maximum in the participation ratio. This window should be dominated by the higher-energy magnons with energy close to the zone-boundary spin waves of the clean system, with only moderate contamination from multimagnon states at even higher energy. We see in Fig. 19(d) that these excitations generate spectral weight rather uniformly over the patches between the vacancies, with typically much less weight on the spins immediately adjacent to the vacancies. This distribution supports our picture of high-energy spin waves that can propagate by several wave lengths before being scattered by the vacancies, though with very substantial damping. The contrast with the spectral weight distribution  $D_2$  of the random network excitations is striking and only partially captured by the participation ratio.

Returning to the window between the random network mode and the high-energy magnons, the map  $D_3$  in Fig. 19(c) essentially interpolates between  $D_2$  and  $D_4$ , with a large concentration of spectral weight on *all* the spins adjacent to vacancies, and essentially uniform smaller weight on other spins. Thus, we conclude that the magnons, in the part of the BZ where the dispersion is anomalous, relatively close to  $\mathbf{q} = (0, 0)$  and  $(\pi, \pi)$ , is affected by the fact that the spins adjacent to impurities have lower mean coupling to the rest of the system. It is also interesting to note that the spins with highest spectral weight in  $D_2$  often have lower weight than other

spins adjacent to vacancies in  $D_3$ . As already discussed, the low-energy magnons also to some extent affect the  $D_2$  map, but the striking difference in spectral weight next to vacancies shows that the excitations are different.

The high-energy magnons will of course also to some extent affect the  $D_3$  map, and it is therefore likely that the low-energy magnons are even more concentrated on the spins with less than four neighbors than what is suggested by the  $D_3$  map. Thus, an effective model involving only this subset of spins may be applicable here, and possibly such an effective model, if suitable interactions could be engineered, may reduce to the previously discussed random network model (including only a subset of the spins with less than four neighbors) at the lowest energy scales.

To summarize what we learn from the real space maps—those shown above and in Appendix B, as well as other cases not shown here—from low to high energy the excitations produce spectral weight as follows: The localized mode ( $D_1$ ) involves the smallest number of spins, most of them adjacent to vacancies and mostly also corresponding to sites with high monomer density. The random network mode ( $D_2$ ) involves a much larger subset of the spins adjacent to vacancies, most of them not belonging to monomer regions. The low-energy magnons ( $D_3$ ) occupy also all the other nearest neighbors of the vacancies and to some extent also uniformly involve the spins in the patches between the vacancies—perhaps less than indicated by  $D_3$ , since it is to some extent contaminated by the high-energy magnons. The high-energy magnons largely avoid the spins closest to the vacancies.

#### IV. QUANTUM ROTOR EXCITATIONS

Here we discuss in more detail the remarkably sharp low-energy peak that we identify as the signature of the lowest state in the tower of Anderson quantum rotor excitations [50]. In a clean system, this state, which has total spin  $S = 1$  for a bipartite lattice with global sublattice balance, is exclusively present in the dynamic structure factor at  $\mathbf{q} = (\pi, \pi)$ . However, as we have seen, in the diluted system there is some rotor weight present for all  $\mathbf{q} \neq (0, 0)$  due to the loss of translational symmetry.  $S(\mathbf{q}, \omega)$  is exactly zero at  $q = 0$  as a consequence of the the conserved uniform magnetization.

##### A. The Anderson rotor tower

Let us first briefly review the mechanism of the quantum rotor tower [50], following the elementary derivation in Ref. 43. In the Néel state, it is assumed that the spins on sublattices A and B effectively form two large spins,  $\mathbf{S}_A$  and  $\mathbf{S}_B$ , with spin quantum numbers  $S_A = S_B \propto N/2$ ,  $N$  being the number of spins. Reduction of the Néel order by quantum fluctuations can be taken into account by setting  $S_A = S_B < N/2$ , but



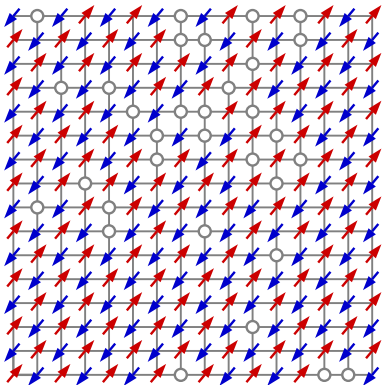


FIG. 20. Illustration of the classical rotor model for a system with vacancies (circles). The spins (arrows) are oriented according to their sublattice, forming a degenerate ground state manifold under global  $O(3)$  rotations.

only the proportionality is important initially. Here we first assume that the system (a large cluster of spins) is sublattice balanced; otherwise  $S_A \neq S_B$ .

The lowest-order rotationally invariant interactions between these spins is

$$H_{\text{eff}} = J_{\text{eff}} \mathbf{S}_A \cdot \mathbf{S}_B = \frac{J_{\text{eff}}}{2} (\mathbf{S} \cdot \mathbf{S} - S_A^2 - S_B^2), \quad (17)$$

where  $\mathbf{S} = \mathbf{S}_A + \mathbf{S}_B$ . Here the  $S = 0$  ground state for  $J_{\text{eff}} > 0$  corresponds to the ordered Néel state and the  $S > 1$  states form the Anderson tower of rotor states, with the terminology reflecting the similarity of the spectrum to that of an actual quantum rotor. Furthermore, since the constant  $-(S_A^2 + S_B^2) \propto N^2$ , we must take  $J_{\text{eff}} \propto 1/N$  for the ground state energy to be proportional to  $N$ . We can therefore write the excitation energy as a function of the total spin  $S$  as

$$E(S) \propto \frac{S(S+1)}{N}, \quad (18)$$

where, the constant of proportionality is the inverse of the transverse uniform susceptibility of the Heisenberg system for a complete match between the effective model and the true eigenvalue spectrum of the model. This matching and numerical tests for the clean 2D Heisenberg model are discussed in detail in Ref. 43, but we do not need the exact matching here.

The  $S_{\mathbf{q}}^z$  operator used in the dynamic spin structure factor can only excite the  $S = 1$  rotor mode from the  $S = 0$  ground state. However, as already discussed, the unbalanced clusters typical in large diluted systems (even when global sublattice balance is imposed) have  $S > 0$  ground states, and the rotor excitations then have spin  $S + 1$  and  $S - 1$ , both of which have energy scaling as  $1/N$ . We confirmed this scaling of the disorder averaged rotor contributions in Fig. 9.

Here our interest is in the way in which the rotor peak at  $\mathbf{q} = (\pi, \pi)$  in the clean system is spread out over the BZ in the diluted system. We find interesting features,

some of which can be explained by classical concepts related to sublattice imbalance and others arising from specific quantum fluctuations that we further explore in Sec. V with the  $J$ - $Q$  model.

In Sec. IV B we first discuss the most basic aspect of nonuniformity at  $\omega = 0$  in the Néel state (which should not be exactly the same as the nonuniformity measured by equal-time correlations) and its rotor weight distribution within a classical model, before presenting our results for the diluted Heisenberg model in Sec. IV C. In IV D we show that some features not captured by the classical rotor model can be naturally explained by the diluted dimer-monomer model. We discuss the distribution of the rotor weight in real space in Sec. IV E.

## B. Classical rotor model

The simplest way to model the distribution of the rotor amplitude in the BZ is with a “classical rotor” model, i.e., treating the spins as classical  $O(3)$  vectors of length  $S_c$  in a Néel configuration, as illustrated in Fig. 20. The degeneracy under rotations can here be interpreted as a zero mode, and the ground states are regarded as eigenstates of the spin operator used in the dynamic spin structure factor. Thus,  $S(\mathbf{q}, \omega)$  only consists of a  $\delta$  function at  $\omega = 0$ . The amplitude of the  $\delta$  function for given  $\mathbf{q}$  is then also the total spectral weight, which equals the static structure factor  $S(\mathbf{q})$ , i.e., the Fourier transform of the equal-time spin-spin correlation function (with the appropriate normalization). Thus, we define the classical rotor weight as

$$W_c^0(\mathbf{q}) = \frac{1}{N} \sum_{\mathbf{r}, \mathbf{r}'} e^{-i\mathbf{q} \cdot (\mathbf{r} - \mathbf{r}')} \langle \mathbf{S}_c(\mathbf{r}) \cdot \mathbf{S}_c(\mathbf{r}') \rangle, \quad (19)$$

where  $\mathbf{S}_c(\mathbf{r}) \cdot \mathbf{S}_c(\mathbf{r}') \in \{0, \pm S_c^2\}$ , depending on the sublattices of  $\mathbf{r}$  and  $\mathbf{r}'$  and the presence of vacancies. The average over vacancy realizations can easily be computed analytically, with the result for  $L \rightarrow \infty$  being

$$W_c^0(\mathbf{q}) = \begin{cases} \pi N (1-p)^2 S_c^2, & \text{for } \mathbf{q} = (\pi, \pi), \\ \pi p (1-p) S_c^2, & \text{for } \mathbf{q} \neq (\pi, \pi), \end{cases} \quad (20)$$

where the factor  $\pi$  comes from its conventional inclusion in the spectral function in Eq. (4). Thus, not surprisingly, we find a divergence with the system size at  $\mathbf{q} = (\pi, \pi)$  and a constant value for other  $\mathbf{q}$ .

We can take some of the quantum effects into account by renormalizing the classical spin length  $S_c$  to the actual sublattice magnetization (per spin, not per lattice site) of the diluted quantum model, which has previously been computed versus  $p$  by SSE simulations [21]. A low-order fit valid for small  $p$  gave

$$S_c \approx 0.3072 - 0.134p - 0.51p^2 \quad (21)$$

in the thermodynamic limit. Finite size effects lead to larger values for smaller  $L$  [21], which we do not take

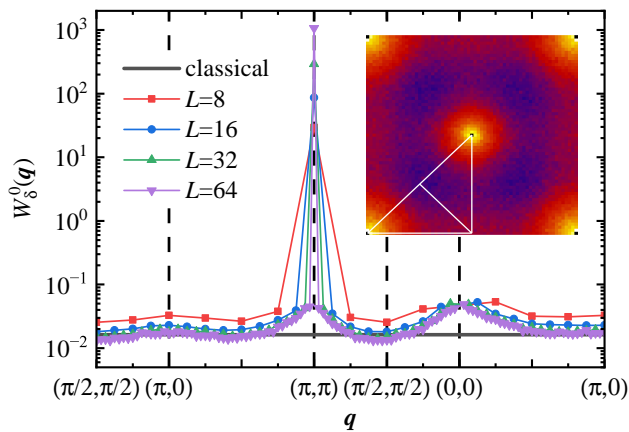


FIG. 21. Distribution of quantum rotor weight at  $p = 1/16$  along a path in the BZ. The horizontal line shows the prediction Eq. (20) of the classical rotor model with the quantum renormalized spin  $S_c = 0.297$ , i.e., the sublattice magnetization per spin according to Eq. (21) [21]. The inset shows the rotor distribution in the entire BZ,  $q_x, q_y \in [0, 2\pi]$ , for  $L = 64$ , with the large weight at  $\mathbf{q} = (\pi, \pi)$  left out. The path in the main graph is marked with lines in the BZ.

into account here but will observe in the results for the Heisenberg model. There is also a small size correction factor  $N/(N-2)$  in the  $\mathbf{q} \neq (\pi, \pi)$  weight that we left out in Eq. (20).

With the proper normalized value of  $S_c$ ,  $W_c^0(\pi, \pi)$  is a strict upper bound of the staggered (long-range) rotor weight in the Heisenberg model in the thermodynamic limit, since it represents the exact value of the full frequency integral of the spectral function, not just its quantum rotor contribution at  $\omega \propto 1/N$ . This bound can be expected to be very accurate, because the quantum rotor weight almost exhausts the divergent static structure factor at  $(\pi, \pi)$ , as can be seen for a small system in Fig. 2(c). At other momenta, where our main interest lays here,  $W_c^0(\mathbf{q})$  should just be taken as a zeroth-order estimate. We would expect larger true rotor weights typically, because the classical Néel state completely neglects the spin fluctuations that give rise to non-trivial correlations for  $\mathbf{q} \neq (\pi, \pi)$  and govern the total spectral weight when used in Eq. (20). The rotor weight is still of course only a small fraction of the total spectral weight for  $\mathbf{q} \neq (\pi, \pi)$ , and just substituting the correct spin correlation function of the diluted Heisenberg model (computed with QMC) would not be of much use here.

### C. Rotor weight in the Heisenberg model

As we saw in Sec. III, the rotor peak for the larger system sizes is well separated from the spectral weight at higher energy. We can therefore define the rotor weight

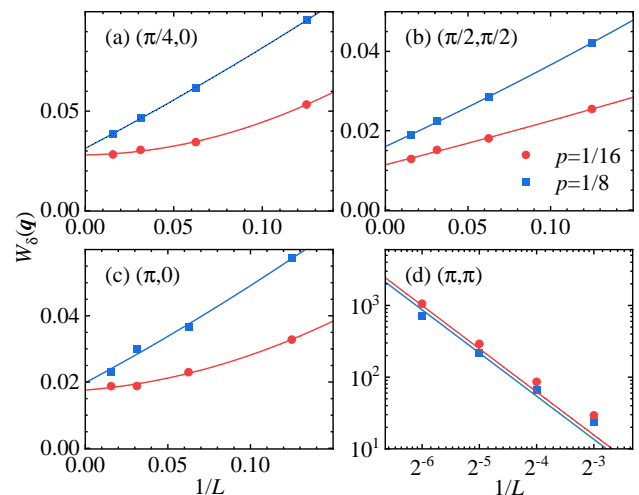


FIG. 22. Size dependence of rotor weight in  $S(\mathbf{q}, \omega)$  at  $p = 1/16$  and  $p = 1/8$  for selected momenta: (a)  $\mathbf{q} = (\pi/4, 0)$ , (b)  $\mathbf{q} = (\pi/2, \pi/2)$ , (c)  $\mathbf{q} = (\pi, 0)$ , and (d)  $\mathbf{q} = (\pi, \pi)$ . In (a)-(c) the curves are fitted second-order polynomials, while in (d) the line corresponds to the predicted form Eq. (20) with the effective spin given by Eq. (21).

as the integral over the sharp peak,

$$W_\delta^0(\mathbf{q}) = \left\langle \int_0^{\text{cut}} S(\mathbf{q}, \omega) d\omega \right\rangle, \quad (22)$$

where the cut-off energy is easily identifiable in our data. Though not visible in the figures in Sec. III, there is some very small spectral weight also between the rotor peak and the localization peak or edge, since no completely sharp features can appear with unrestricted sampling in SAC and there is also likely an actual thin low-energy tail of the localization peak. Therefore, a minimum exists that can be taken as the cut-off  $\omega$  value in the integral. The value of  $S(\mathbf{q}, \omega)$  at the cut-off is typically orders of magnitude below the weight at the localization edge, and the results of the integral in Eq. (22) is insensitive to the details of how the cut-off is chosen.

In Fig. 21 we graph the resulting rotor weight along our standard path in the BZ for different system sizes. Here we use a log scale on the vertical axis in order to visualize both the divergent weight exactly at  $\mathbf{q} = (\pi, \pi)$  and the distribution of convergent weight over the rest of the BZ. Overall, for  $\mathbf{q} \neq (\pi, \pi)$  we observe slowly decreasing rotor weight with increasing  $L$ , with only minor differences in the results for  $L = 32$  and  $L = 64$ . Instead of the uniform weight in the classical model for  $\mathbf{q} \neq (\pi, \pi)$ , we see accumulation of weight close to both  $(\pi, \pi)$  and  $(0, 0)$ , with a minimum close to (not exactly at)  $(\pi/2, \pi/2)$ . In this region the weight falls below the constant value predicted using the classical rotor model, while at other momenta it is much higher.

In Fig. 22 we analyze the size dependence of the rotor weight at selected momenta for both  $p = 1/16$  and  $p = 1/8$ . In some cases the size correction is very close to

$R_m \backslash N_m$	0	2	4	6	8	...	$\bar{N}_m$
32	983	17	0	0	0	0	0.034
40	957	38	5	0	0	0	0.096
48	830	120	33	11	5	1	0.49
64	336	246	172	112	60	74	3.182

TABLE I. Number of realizations  $R_m$  with  $N_m$  monomers remaining in equilibrium in the dimer-monomer model with vacancy fraction  $p = 1/16$  when a total of 1000 vacancy realizations were generated. Results are shown versus the system size, and in each case the mean value of monomers is shown in the rightmost column. The  $\dots$  column includes all  $N_m > 8$ .

linear in  $1/L$ , while at generic points a quadratic fit works well. At  $(\pi, \pi)$  we see the expected linear divergence in  $N$ , with the exact form very close to the prediction based on Eq. (20) when the values of  $S_c$  corresponding to  $p = 1/16$  and  $1/8$  are taken according to Eq. (21). For the other  $\mathbf{q}$  points, we do not have any further insights in the size dependence expected, but it is nevertheless clear from the results that the nonuniform rotor weight distribution persists in the thermodynamic limit.

In the inset of Fig. 21 we show a heat map of the weight in the entire BZ, where a broad minimum around  $(\pi/2, \pi/2)$  (and the three other symmetrically located points) is also apparent. Note again that there is no spectral weight at all at  $(0,0)$ , and in the heat map we have also left out  $(\pi, \pi)$  since the rotor weight there is orders of magnitude larger than at nearby points.

When translated to real space, the rotor weight distribution reflects a certain nonuniformity in the breaking of the spin rotational symmetry in the Néel state. It should be noted here again that the equal-time spin-spin correlation function, i.e., the static structure factor  $S(\mathbf{q})$ , corresponds to the total spectral weight for given  $\mathbf{q}$ , but the rotor weight is only the static,  $\omega = 0$  (when  $L \rightarrow \infty$ ), contribution. At  $\mathbf{q} = (\pi, \pi)$ , the equal-time and static structure factors are essentially the same, as we discussed above and illustrated in Fig. 22(d). However, at other momenta the rotor amplitude is only a fraction of the static structure factor. It should still in principle be possible to detect these contributions experimentally using elastic neutron scattering, in particular the broadened  $\mathbf{q} = (\pi, \pi)$  Bragg peak and the new peak at  $\mathbf{q} = (0, 0)$ ,

We will go through several steps of trying to understand the origins of this  $\omega = 0$  spin texture, in the subsections below and further in Sec. V with the aid of the  $J$ - $Q$  model, where the suppression of weight around  $(\pi/2, \pi/2)$  is amplified by the four-spin interaction  $Q$ .

#### D. Dimer-monomer model

We here explore the ability of the classical dimer-monomer model to generate features of the rotor weight

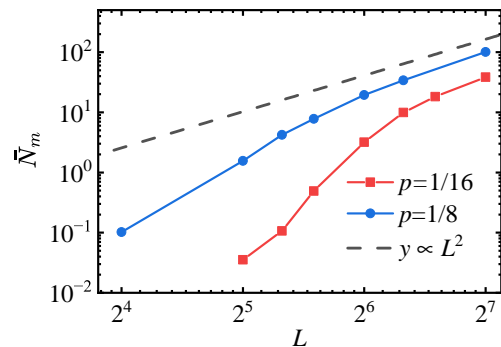


FIG. 23. Average monomer number vs system size for  $p = 1/16$  (red squares) and  $p = 1/8$  (blue circles). The dashed line shows qualitatively the expected linear growth with the system volume.

related to local sublattice imbalance. We already showed an example of enhanced local magnetic response matching regions of local sublattice imbalance in the dimer model in Fig. 6, following the approach first used to model the 2D Heisenberg model when diluted close to the percolation point ( $p_c \approx 0.407$ ) in Ref. 28.

We consider configurations with the minimum number of monomers for each random realization, sampled with the algorithm explained in Fig. 4. To reduce statistical fluctuations for small system sizes, we again use a canonical ensemble for the vacancy fraction, i.e., for system size  $N = L^2$ , the number of vacancies is exactly  $pN$ . For small systems, the number of remaining monomers is often zero, and we generate a large number of configurations in order to obtain sensible averaged results. Table I shows examples of the distribution of the number of remaining monomers in system sizes up to  $L = 64$ . It is only for system sizes larger than  $L = 64$  that the expected mean number of monomers grows in proportion to the system volume, as seen in Fig. 23.

Regarding the monomers as spins  $S_r = \pm 1/2$  according to their sublattices, as in Fig. 5, we again perform a Fourier transform similar to Eq. (19) in the classical rotor model,

$$F(\mathbf{q}) = \frac{1}{\bar{N}_m} \left| \sum_{\mathbf{r}_m} S_{\mathbf{r}_m} e^{-i\mathbf{q} \cdot \mathbf{r}_m} \right|^2 \quad (23)$$

where  $\mathbf{r}_m$  are the positions of monomers.

The idea behind the dimer-monomer model in this context is that the sublattice imbalance described by the monomers enhance the staggered magnetic order relative to the renormalized flat Néel background described by  $S_c$  in Eq. (21). Recall that we used a value for the classical spin length  $S_c < 1/2$  to account for the quantum fluctuations that reduce the magnitude of the Néel order parameter. The monomer regions can now be regarded as locally enhanced Néel order, i.e., larger  $S_c$ , in (an unknown) proportion to the monomer density. The so generated nonuniform Néel state will lead to deviations from the zeroth-order predictions in Eq. (20). The

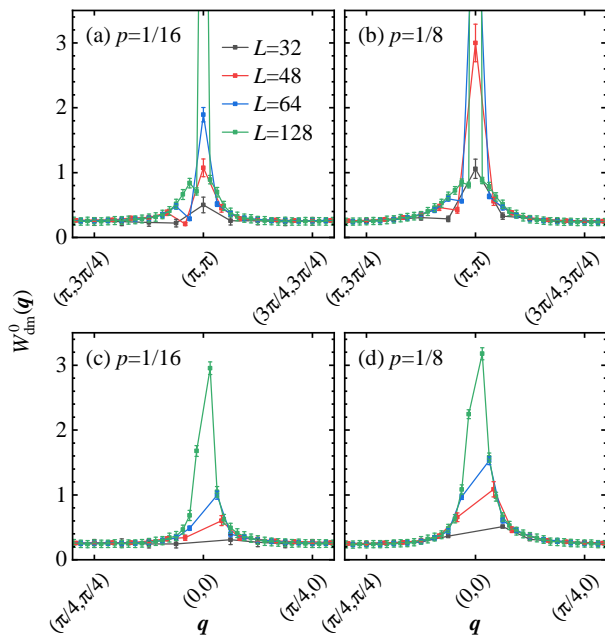


FIG. 24. Rotor weight distribution obtained with the dimer-monomer model near  $\mathbf{q} = (\pi, \pi)$  and  $(0, 0)$ . Further away from these points the value does not change appreciably. Results for  $p = 1/16$  are shown in (a) and (b), while (c) and (d) show analogous results for  $p = 1/8$ .

results for the dimer-monomer model will only represent these differences. Thus, we define the additional weight of the rotor state in momentum space as

$$W_{\text{dm}}^0(\mathbf{q}) = \langle F(\mathbf{q}) \rangle, \quad (24)$$

with  $F(\mathbf{q})$  defined in Eq. (23) and averaged over large number of dimer-monomer configurations for each vacancy realization, and further averaged over several thousand vacancy relations for small  $L$  and about 1000 for the largest  $L$  considered.

We show results for several system sizes at both  $p = 1/16$  and  $p = 1/8$  in Fig. 24. Here we observe two prominent features that are absent in the classical rotor model: (i) weight spreads out from the  $\delta$  function at  $\mathbf{q} = (\pi, \pi)$  to form a broadened peak, and (ii) a second peak has emerged at  $(0, 0)$ , which is somewhat broader than the  $(\pi, \pi)$  peak. The value exactly at  $(0, 0)$  is zero because of the imposed global sublattice balance. These two peak features both agree qualitatively with the results for the rotor weight in the Heisenberg model in Fig. 21, and we can therefore conclude that they indeed reflect the consequences of sublattice imbalance as modeled by the dimer-model model. Importantly, however, the dimer-monomer model does not produce any other structure in the BZ beyond the two peaks; in particular, the differences between the zone-boundary points  $\mathbf{q} = (\pi/2, \pi/2)$  and  $(\pi, 0)$  in Fig. 21 are not reproduced within the classical dimer-monomer model.

In attempts to explain this missing features, we have also carried out simulations with dimer-dimer interac-

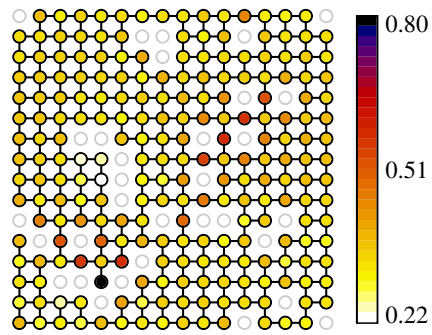


FIG. 25. Rotor weight distribution  $D_0(\mathbf{r})$  in real space in the same  $L = 16$  system as in Fig. 6, computed according to Eq. (15) in an energy window similar to that indicated for an  $L = 32$  system in Fig. 18.

tions included, the motivation being that the Heisenberg model already shows precursors to the formation of a columnar valence-bond solid state, one manifestation of which is the dip in magnon energy close to  $\mathbf{q} = (\pi, 0)$  seen in Fig. 12 [36]. As shown in Appendix C, the results in Fig. 24 are rather stable, however, and neither attractive nor repulsive columnar dimer interactions can generate the sought effect. Thus, we believe that the suppression of  $(\pi/2, \pi/2)$  weight (where the minimum is actually not exactly at this  $\mathbf{q}$  point) is a manifestly quantum dynamical effect, which we explore in Sec. V with the  $J$ - $Q$  model.

### E. Rotor weight in real space

We now return to the real-space distribution of spectral weight discussed in Sec. III D, considering the window including only the quantum rotor excitation in Eq. (15). We here use the same  $L = 16$  vacancy realization as in Fig. 6, and in Appendix B we show supporting results for the same  $L = 32$  realization as in Fig. 19. The  $\mathbf{r}$  averaged spectral weight  $S_0(\omega)$  of the  $L = 16$  sample looks qualitatively similar to that for the  $L = 32$  sample in Fig. 18, and we define the energy window  $D_0(\mathbf{r})$  in the same manner so that it contains only the rotor peak.

The real-space distribution  $D_0$ , shown in Fig. 25, looks very similar to the local susceptibility map in Fig. 6(a). This can be explained by the well-known sum rule for the local susceptibility (see, e.g., Ref. [28]),

$$\chi_{\mathbf{r}} = \frac{2}{\pi} \int_0^\infty \frac{S(\mathbf{r}, \omega)}{\omega} d\omega, \quad (25)$$

which implies that excitations at the lowest energies will dominate, provided that they carry significant spectral weight. A robust rotor peak indeed always exists at energy far below the spectral weight in the continuum at higher energies. Thus, the rotor weight should be expected to contribute significantly to  $\chi_{\mathbf{r}}$ .

Given the close match between the results in Fig. 25 and the monomer distribution in Fig. 6(b), we conclude



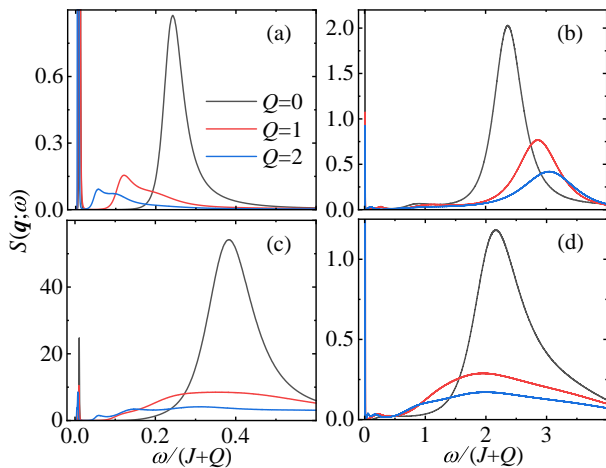


FIG. 26.  $S(\mathbf{q}, \omega)$  at  $p = 1/16$ ,  $L = 32$ , computed with the  $J$ - $Q$  model at  $Q/J = 0$  (black curves), 1 (red), and 2 (blue) at representative  $\mathbf{q}$  points: (a)  $\mathbf{q} = (2\pi/L, 0)$ , (b)  $\mathbf{q} = (\pi/2, \pi/2)$ , (c)  $\mathbf{q} = (\pi - 2\pi/L, \pi - 2\pi/L)$ , (d)  $\mathbf{q} = (\pi, 0)$ .

that the dimer-monomer model is a good indicator for the spatial distribution of the quantum rotor state, which is also of course the prerequisite for using it to explain the rotor weight distribution in  $\mathbf{q}$  space above in Sec. IV D.

We show both the monomer and rotor weight distribution for the same  $p = 1/8$ ,  $L = 32$  vacancy realization as in Fig. 19 in Appendix B, and also similar results for a case of  $p = 1/16$ . Here again we find a strong correlation between monomer sites and rotor weight, with the rotor weight also being large at all other sites (as is also the case in the  $L = 16$  case in Fig. 25), as expected because all spins participate in the Néel ordering and the monomer sites only reflect elevated  $\omega = 0$  ordering. The localized excitations, corresponding to the energy window above the rotor peak, visualized in the map in Fig. 19(a), also have strong overlap with some of the monomer sites, but much lower spectral weight overall is distributed on the other spins.

## V. J-Q MODEL

As we have seen above, the difference in rotor weight at  $\mathbf{q} = (\pi, 0)$  and  $\mathbf{q} = (\pi/2, \pi/2)$  cannot be accounted for simply by sublattice imbalance as described by the classical rotor model supplemented by the dimer-monomer model. This deficit of the semi-classical description of the Néel state, with suppression of the overall Néel order by quantum fluctuations and local enhancement in regions of sublattice imbalance, is not surprising in itself. However, the particular effect of suppression of the rotor weight close to  $\mathbf{q} = (\pi/2, \pi/2)$  may be related to the same mechanism that increases the magnon energy at this momentum while reducing it at  $(\pi, 0)$ , as observed both in the clean and diluted systems in Fig. 13.

This effect on the dispersion relation was shown to

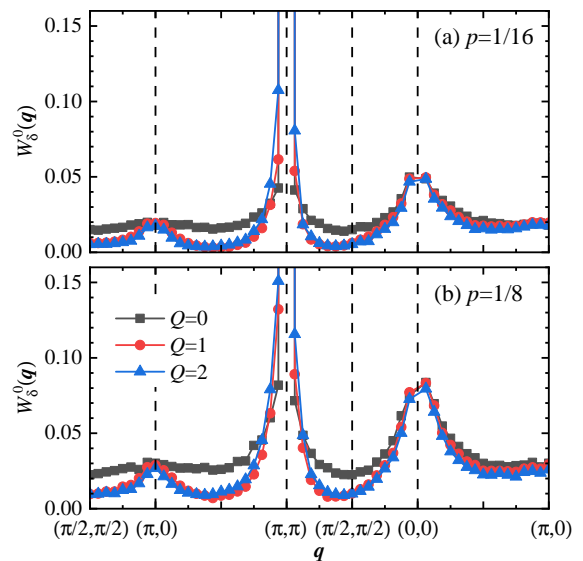


FIG. 27. Rotor weight distribution in the  $L = 32$   $J$ - $Q$  model with  $Q/J = 0$  (black squares), 1 (red circles), and 2 (blue triangles), graphed along the standard path in the BZ at vacancy fraction  $p = 1/16$  in (a) and  $p = 1/8$  in (b).

originate in quantum fluctuations related to incipient spinon deconfinement close to  $\mathbf{q} = (\pi, 0)$  [36], a conclusion reached for the clean system by monitoring the effects the four-spin interaction  $Q$  in the  $J$ - $Q$  model defined in Eq. (3). It was found that the magnon peak in  $S(\mathbf{q}, \omega)$  at  $\mathbf{q} = (\pi, 0)$  vanishes or becomes extremely small already when  $Q/J = 1$ , far below the quantum phase transition into a valence-bond solid state at  $Q/J \approx 22$  [40]. In contrast, the magnon peak remains robust at  $\mathbf{q} = (\pi/2, \pi/2)$ . Here we use the  $J$ - $Q$  model for the same purpose to investigate the effects of enhanced correlated singlet fluctuations on the distribution of the rotor weight in the BZ.

In Fig. 26 we show the dynamic structure factor at  $p = 1/16$  in a system of size  $L = 32$  at selected momenta, comparing results for  $Q/J = 0, 1$ , and 2. In all cases except for  $\mathbf{q} = (\pi/2, \pi/2)$ , the location of the most prominent peak is shifted dramatically to lower energy when  $Q$  increases. A large quantum rotor peak persists at  $Q > 0$ , as it should since the system is still strongly Néel ordered at these values of  $Q$ . Much more continuum spectral weight extends to low energies, ending at a small peak far below the energy of the localization edge for this system size at  $Q = 0$  (Fig. 15). Thus, it appears that the  $Q$  interaction further facilitates the formation of a low-energy localization mode—perhaps in this case reflecting localized spinons. In contrast to the other momenta, at  $\mathbf{q} = (\pi/2, \pi/2)$  in Fig. 26(b) the high-energy mode remains with significant spectral weight and its energy increases, as in the clean system [36].

In Fig. 27 the weight of the quantum rotor peak is graphed along the standard path in the BZ for both  $p = 1/16$  and  $p = 1/8$  and for the same three values

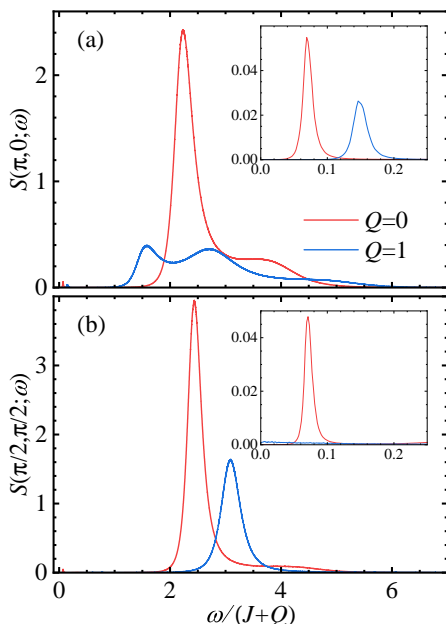


FIG. 28. Dynamic structure factor in the  $L = 16$  Heisenberg model ( $Q = 0$ ) and  $J$ - $Q$  model ( $Q = 1$ ), both with one vacancy and shown for  $\mathbf{q} = (\pi, 0)$  in (a) and  $\mathbf{q} = (\pi/2, \pi/2)$  in (b). The insets focus on the quantum rotor peaks, which in (a) have weight  $W_\delta^0 \approx 0.0011$  at  $Q = 0$  and  $W_\delta^0 \approx 0.0015$  at  $Q = 1$ . In (b)  $W_\delta^0 \approx 0.0008$  at  $Q = 0$ , while at  $Q = 1$  a much smaller spectral weight is spread out between  $\omega = 0$  and  $\omega \approx 0.1$  and does not form a sharp peak.

of  $Q/J$  as above. Here the depletion of the weight close to  $(\pi/2, \pi/2)$  is obviously much more dramatic at  $Q = 1$  than at  $Q = 0$ , with not much further change when increasing  $Q/J$  to 2. An interesting feature here is that the suppression is actually stronger at the lower vacancy fraction. This counter-intuitive result has its natural explanation in our proposed mechanism: The precursor fluctuations related to spinon deconfinement, i.e., correlated singlets resonating in columnar patterns, which reflect the eventual transition to the columnar dimerized state at large  $Q/J$ . At the larger vacancy fraction, these extended fluctuations of the bulk are to some extent already hindered by the presence of the vacancies, which individually favor certain vortex-like patterns (at least for large  $Q/J$ ) [56] and collectively prohibit the formation of a uniform pattern in the dimerized phase [57].

Our assertion that the  $Q$ -enhanced singlet fluctuations are responsible for the suppression of rotor weight at  $\mathbf{q} = (\pi/2, \pi/2)$  is further supported by results for systems with one and two vacancies, shown in Figs. 28 and 29, respectively. Comparing results at  $Q/J = 0$  and 1 for a small system,  $L = 16$ , we again see completely different effects of the  $Q$  interaction at  $\mathbf{q} = (\pi, 0)$  and  $(\pi/2, \pi/2)$ , with the magnon peak pushed up in energy by  $Q$  in the latter case while the spectral weight instead broadens out to lower energies in the former case. The rotor weight increases slightly with  $Q$  at  $\mathbf{q} = (\pi, 0)$  but is diminished at

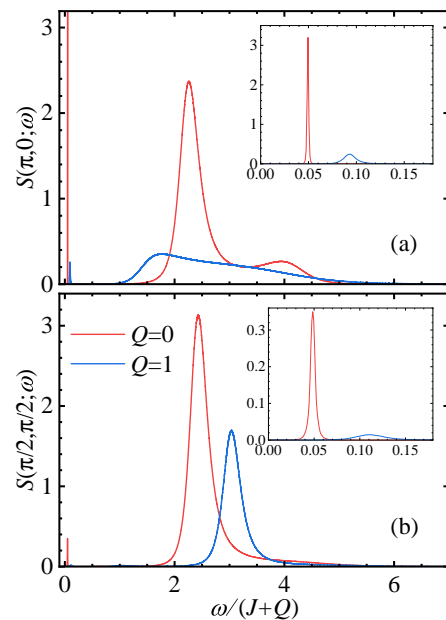


FIG. 29. Results as in Fig. 28 but for two vacancies at maximum separation. The rotor weight in (a) is  $W_\delta^0 \approx 0.0066$  at  $Q = 0$  and  $W_\delta^0 \approx 0.0089$  at  $Q = 1$ , while in (b)  $W_\delta^0 \approx 0.0025$  at  $Q = 0$  and  $W_\delta^0 \approx 0.0014$  at  $Q = 1$ .

$\mathbf{q} = (\pi/2, \pi/2)$ . In most of the cases, the rotor energy is higher when  $Q/J = 1$ , which also explains the more significant broadening of the peak by the SAC. However, in the case of the single vacancy, the  $(\pi/2, \pi/2)$  rotor weight in Fig. 28(b) is extremely small and spread out over a wide range of low energies, which may just be an effect of the weight being too small to resolve properly.

The main message of all these results for the  $J$ - $Q$  model is that the precursor fluctuations to spinon deconfinement in the clean Heisenberg model and  $J$ - $Q$  model with small  $Q$  are also responsible for the depletion of the rotor weight at  $\mathbf{q} = (\pi/2, \pi/2)$  in the diluted system. This depletion, which reflects a nonuniform spin texture at  $\omega = 0$  in the Néel state, may possibly be experimentally detectable by elastic neutron scattering in layered antiferromagnets doped by nonmagnetic impurities [5], though the effect is rather weak in the Heisenberg model. The peak around  $\mathbf{q} = (0, 0)$  may be easier to detect but is not related to the spinon precursor.

## VI. CONCLUSIONS AND DISCUSSION

### A. Brief summary of main results

By studying the disorder averaged dynamic structure factor  $S(\mathbf{q}, \omega)$  using state-of-the-art QMC and SAC methods, we have obtained a wealth of insights into the excitations of the 2D Heisenberg model diluted with vacancies. In total, we identified six different types of excitations forming a multiscale structure factor. Some of our

observations were previously predicted in spin wave theory with a  $T$ -matrix approach for the vacancies. Specifically, localized excitation at a low energy [15] and a high-energy magnon with dispersion relation close to that in the clean system, crossing over to an anomalous dispersion relation at lower energies above the localization energy [9, 15]. However, there are both quantitative and qualitative discrepancies.

Most importantly, we found a second previously missed propagating “random network” mode at energy below the spin waves and novel aspects of the quantum rotor excitation associated with the formation of the long-range Néel order in the thermodynamic limit. Finally, there is a significant multimagnon continuum for all  $\mathbf{q}$ , extending as far as to  $\omega \approx 5$  at the zone boundary.

The energy  $\omega_{\text{loc}} \propto e^{-\pi/4p}$  of the localized mode was obtained in Ref. 15 at small dilution fractions  $p$ . At  $p = 1/8$ , we were able to extrapolate the energy of the localization mode to infinite system size, giving  $\omega_{\text{loc}} \approx 0.1$ , which is about 50 times larger than the predicted energy scale. At  $p = 1/16$ , the localization energy is too low for a meaningful extrapolation with the system sizes available, but the trend of our data versus  $1/L$  is to a value clearly below that for  $p = 1/8$ .

As for the discrepancy at  $p = 1/8$ , it should be noted that the prefactor of the exponential form of  $\omega_{\text{loc}}$  was not calculated analytically, and the form also perhaps applies only at much smaller dilution fractions. It is also possible that the localized excitation found here is not exactly of the same type as in the analytical calculation, because of the approximations made there.

The real-space resolved structure factor  $S(\mathbf{r}, \omega)$  proved to be very useful in further characterizing the excitations by the manner in which individual spins participate in production of spectral weight within different energy windows. In particular, using this tomographic approach, we conclude that some of the spins located at sites in the immediate vicinity (nearest neighbors) of the vacancies form a subsystem—a random network of interacting moments—that is mainly involved in the low-energy propagating mode. In contrast, the magnons generate almost uniform spectral weight in the patches between vacancies, with much less weight on the spins adjacent to vacancies at high energy. At lower energy, where the dispersion relation becomes anomalous, close to the predicted logarithmic form [15], the spectral weight is the largest on the spins adjacent to the vacancies.

Because of these qualitative differences between low- and high-energy magnons, we regard them as two different types of excitations within their respective energy windows. As the energy is further lowered toward that of the random network mode, the weight between the vacancies diminishes, and also on the majority of the spins next to vacancies, thus leaving behind the rather sparse random network of spins with large spectral weight. This energy window is also to some extent influenced by the tail of the low-energy magnons, and the observed uniform weight within the patches may to a large extent

arise from these excitations, for which we find further support in the fact that the participation ratio decreases when  $\omega$  is lowered.

The quantum rotor excitation is not included in spin wave calculations, where the  $O(3)$  symmetry of the Néel order parameter is broken from the outset. In a finite system, the symmetry is not broken and the tower of  $S > 0$  states that become degenerate in the thermodynamic limit (which can combine to form the symmetry-broken state) is present in the excitation spectrum. An important aspect of our work was to investigate how the rotor weight in the dynamic structure factor at  $\omega \propto 1/N$  spreads out in momentum space from  $\mathbf{q} = (\pi, \pi)$ , where it is located in the uniform system. We found broadened peaks close to both  $(\pi, \pi)$  and  $(0, 0)$ , which can be explained by local sublattice imbalance modeled by a simple classical dimer-monomer model. Other structure, specifically a depletion of spectral weight close to  $\mathbf{q} = (\pi/2, \pi/2)$ , can be magnified by turning on the four spin interaction of the  $J$ - $Q$  model, thus suggesting signatures of incipient spinon deconfinement at momenta close to  $\mathbf{q} = (\pi, 0)$ , similar to the clean 2D Heisenberg model [36]. We also found an enhanced tendency of localization in the  $J$ - $Q$  model.

## B. Contrasts with spin wave theory

Spin waves with anomalous dispersion had been predicted early on [7, 9, 10] but it was only the work of Chernyshev et al. [15] that resolved the way in which this mode merges with localized state at low energy. Thus, very close to  $\mathbf{q} = (0, 0)$  and  $(\pi, \pi)$ , the use of a disorder averaged medium, in which the spin waves propagate at higher energy, becomes invalid. However, the relationship between the anomalous spin waves and essentially conventional magnons (in reality highly damped) at higher energy remained unsettled, as the interactions between the spin waves of the clean system and the impurity modes (from the spins next to vacancies) at energy  $\omega \approx J$  was not sufficiently included to obtain reliable spectral functions at these energies. The high-energy mode then exists as an apparently well defined separate excitation close to the magnetic zone boundary. In some parts of the BZ (where the magnon energy is of order  $J$ ), they both exist as individual excitations, producing two separate peaks in  $S(\mathbf{q}, \omega)$ . In our calculations, we always observe only one peak at these energy scales. In the spin wave theory there is also no propagating mode in the  $(\mathbf{q}, \omega)$  regions where we identify the random network excitations.

Our calculations differ in a fundamental manner from the  $T$ -matrix calculations, in that we perform the disorder average of the dynamic correlation function (in imaginary time) and do not assume that the excitations are formed in an already averaged medium. As already mentioned above, we demonstrated that the excitations below the anomalous magnon actually propagate only within a

subset of the spins; a fraction of those in the closest vicinity of (distance one lattice spacing from) the vacancies. We conjecture that these spins form a random network of moments coupled to each other by an effective interaction much less than  $J$ . It is likely that disorder averaging at the early stage in the  $T$ -matrix approach excludes this type of excitation from the outset.

There is an alternative to the disorder averaged medium with the  $T$ -matrix in spin wave theory: the linear spin wave Hamiltonian can be diagonalized numerically in real space for specific disorder realizations and then averaged [16]. This approach is closer to our work in terms of the way the disorder averaging is carried out. However, it appears that the linear spin wave Hamiltonian is not sufficient to describe the different excitation modes accurately, as the dynamic structure factor at low dilution (computed for system size  $L = 32$ ) is essentially a double peak below the zone boundary energy [16], with neither signs of a lower-energy propagating mode (which in our calculation is far below the lower of the two almost joined peaks in the spin wave calculation) nor a localization peak at low energy. Overall, the profile for momenta close to the zone boundary is much more broadened by disorder than in the  $T$ -matrix approach, though still lacking the high-energy (multimagnon) tails that we have found here. Thus, we conclude that the interactions neglected within linear spin wave theory (which also is the starting point of the  $T$ -matrix calculations) are crucial in forming the true excitations of the diluted Heisenberg model.

The lack in the numerical spin wave calculation of features seen in the  $T$ -matrix calculation [15] is surprising, given that the exact diagonalization of the linear spin wave Hamiltonian in principle contains all the processes of the  $T$ -matrix approach, and also the multi-impurity scattering processes neglected there. Perhaps the spectral weight of the localization feature only appears for larger system sizes within linear spin wave theory, while in our fully interacting systems it appear sooner. As mentioned, it is also possible that the localization mode within the  $T$ -matrix approach is different, from both our calculations here as well as the exact spin wave diagonalization, because of the impurity averaged medium.

### C. Relevance of the dimer-monomer model

An important remaining question is how, or even if, the 2D monomer percolation transition at  $p_c = 0$  (at  $p_c > 0$  in three dimensions) in the dimer-monomer model [31] is related to the localization mode of the Heisenberg model. Superficially, if the monomer regions correspond to spins involved in the localization process, then the size of these regions diverges as  $p \rightarrow 0$  and the excitation energy approaches 0. The lowering of the localization mode in the  $T$ -matrix analysis is exponentially rapid as  $p$  is decreased,  $\omega_{\text{loc}} \propto e^{-\pi/4p}$  [15], while the percolation phenomenon is associated with critical (power law) behavior (with, e.g.,

an unusually large correlation length exponent,  $\nu \approx 5$  [31]). This difference is not necessarily a contradiction, because more than one monomer region may be involved in a low-energy excitation. The localization length scale is therefore not necessarily that of a single domain of spins, but may instead reflect a typical distance between far separated groups of small numbers of spins.

From our real-space results in Sec. IV, it is clear that the monomer regions correlate strongly with the spectral weight distribution of the rotor mode. However, all the spins carry substantial relative spectral weight of the rotor mode—which is natural since the entire system is affected by the Néel order and participate in the symmetry breaking. There is only elevated weight on the monomer sites (and some other sites) reflecting a real-space texture of the Néel state as observed at zero frequency (corresponding to inelastic neutron scattering). This texture is different from that manifested in the equal-time spin correlation function, which corresponds to the entire spectral weight integrated over frequency.

The monomer regions also correlate strongly with the localized excitations, as shown in Sec. IIID and Appendix B, but in this case there is significant spectral weight only on some of the monomer rich sites, and almost no spectral weight is carried by spins not belonging to monomer regions. Since there are likely many large localized excitations in a given sample and our tomographic approach only reflects their collective impact on the spins, it is not possible to draw any quantitative conclusions on the number of spins involved in a single localized state. Our system sizes are also too small to fully contain even one typical localized state (though at  $p = 1/8$  the  $L = 64$  value of  $\omega_{\text{loc}}$  is already close to the extrapolated value). Nevertheless, the fact that the monomer sites are strongly matched with the low-energy states above the quantum rotor suggests that the localized mode in some way is dominated by a rather small number of weakly interacting spins belonging to regions of sublattice imbalance in the dimer-monomer model.

More broadly, our real-space tomographic analysis suggests that the excitations are gradually concentrated on the spins immediately adjacent to the vacancies as the energy is lowered from the zone boundary energy. Some of these spins become “deactivated” as the energy approaches that of the low-energy spin waves, and finally the localized states involves only a very small subset of those spins. Therefore, the most likely interpretation of the length scale associated with the localized mode is one characterizing the distance between spins within that subset of effective moments in different parts of the lattice, not the size of a single connected patch of a large number of spins. Thus, it appears that the localized states may be related to the dimer-monomer model, but exactly how remains an open question.

A natural step in the future would be to construct an effective model containing only the spins adjacent to vacancies, with suitable interactions between disconnected groups of spins and also couplings to a global staggered



field. Such a model may possibly describe the anomalous magnons as well as the random network mode (where most of the spins have been frozen out) and also the localized mode. However, it is not clear from the outset how to incorporate the local sublattice imbalance within this framework. Effective models would not only be useful both for computational studies on larger length scales, but also in analytical work to further elucidate the nature of the excitations.

Since a monomer percolation transition at  $p_c > 0$  was predicted in three dimensions [31], it would be interesting to repeat the kind of calculations we have reported here for the 3D diluted Heisenberg model. A direct connection between monomer regions and localized excitations would then imply a transition at  $p > 0$  from a gapless spin conductor to a disordered spin insulator with gapped localized excitations at  $T = 0$ .

#### D. Experimental significance

While there have been substantial past experimental studies of cuprate square-lattice antiferromagnets (parent compounds of high- $T_c$  superconductors) with Cu substituted by Zn and Mg [1–6], the focus was typically on the effects of vacancies on the long-range Néel order and on dynamic and thermodynamic properties at rather high temperatures. The NQR relaxation experiments in Ref. 3 are intriguing in our context here, because a low-energy peak was detected at low temperatures, shifting down with  $p$ , which was not compatible with the energy expected for conventional spin waves and was instead interpreted as a “freezing” of local moments. In light of our results here and in Refs. [9, 15], the peak could possibly reflect the damped propagating low-energy excitations of the random spin network.

The best experimental realization of the 2D Heisenberg model to date is  $\text{Cu}(\text{DCOO})_2 \cdot 4\text{D}_2\text{O}$  [35], which could also possibly be doped by Zn or Mg (replacing Cu as in the cuprates). Most likely, this would also correspond to vacancies in the Heisenberg model. It should be noted that such substitutions can also lead to modifications of the exchange interactions around the nonmagnetic sites, which has detectable consequences in the Néel ordered moment versus  $p$  [17, 18]. The weakly modified interactions would certainly also lead to quantitative shifts in the excitations discussed here, but we expect all types of excitation modes to still be present. In  $\text{Cu}(\text{DCOO})_2 \cdot 4\text{D}_2\text{O}$  the exchange constant is approximately 70 K, more than an order of magnitude smaller than in the cuprates. Thus, the spin dynamics is more easily accessible in neutron scattering experiments over the full magnetic bandwidth. The cuprates also are known to have more effects of ring-exchange and other higher-order interactions when the spin-only model is derived from the Hubbard model [62, 63].  $\text{Cu}(\text{DCOO})_2 \cdot 4\text{D}_2\text{O}$  doped with Zn or Mg may be the best realization also of the site diluted Heisenberg

model, if such compounds are stable.

The peak formed in  $S(\mathbf{q}, \omega)$  in the model at the low localization scale may in principle be observable in NMR experiments at low  $p$  in the form of the dependence of the spin-lattice relaxation rate  $1/T_1$  on the nuclear resonance frequency  $\omega_N$ , since  $1/T_1 \propto S_0(\omega_N)$  (with idealized on-site only hyperfine couplings). However, it is not clear from our  $T = 0$  work how finite-temperature effects (and also magnetic field effects in NMR experiments) will affect the likely fragile spectral weight structure at this very low energy scale. Overall, neutron scattering experiments at dilution fractions  $p \sim 10\text{-}20\%$  may be more realistic, if sufficiently low temperature can be reached.

With the  $T = 0$  results for the diluted Heisenberg model at hand, to connect more closely to materials and experiments it would be useful to also carry out  $T > 0$  QMC calculations, of the spectral functions studied here and also of low-temperature thermodynamics. In addition to the single layer, the expected weak interlayer couplings present in materials can also be taken into account, though of course the larger volume also makes the simulations more demanding of computing resources—the calculations presented here already consumed about five million CPU hours.

A promising simplified way to include the effects of 3D Néel order at low temperature is to add a weak staggered magnetic field to the Hamiltonian Eq. (2), to break the spin-rotation symmetry of the order parameter. This symmetry breaking also enables the separation of the transversal and longitudinal components of  $S(\mathbf{q}, \omega)$  (which can be experimentally separated with polarized neutrons). This approach was taken in an early QMC and numerical analytic continuation study of the 2D Heisenberg model [34] and can be repeated, now with more powerful analytic continuation tools, for diluted systems at not much more computational effort than in the work on the rotationally symmetric model studied here.

#### E. Technical aspects

On a technical level, the spectral functions resolved here are unprecedented, as far as we know, in their rich details at energy scales ranging from  $\omega \approx 10^{-3} J$  to  $\omega \approx 5J$ . Looking at the local spectral functions in Fig. 15, there are five distinct peaks, each of which we have explained in terms of the different types of excitations discussed above. The ability to resolve structure at low energy is related to the very low temperatures used in the QMC simulations; typically  $T = 1/4N$ . With such low temperatures, and with excitations present down to a similar energy scale, the imaginary-time correlations  $G(\tau)$  remain significant within statistical errors up to  $\tau$  of order 4000 for the largest system size, thus containing a large amount of information that can be converted to the frequency domain using the SAC method.

Our results should serve as an example of the possibility to reach these very low temperatures and resolve

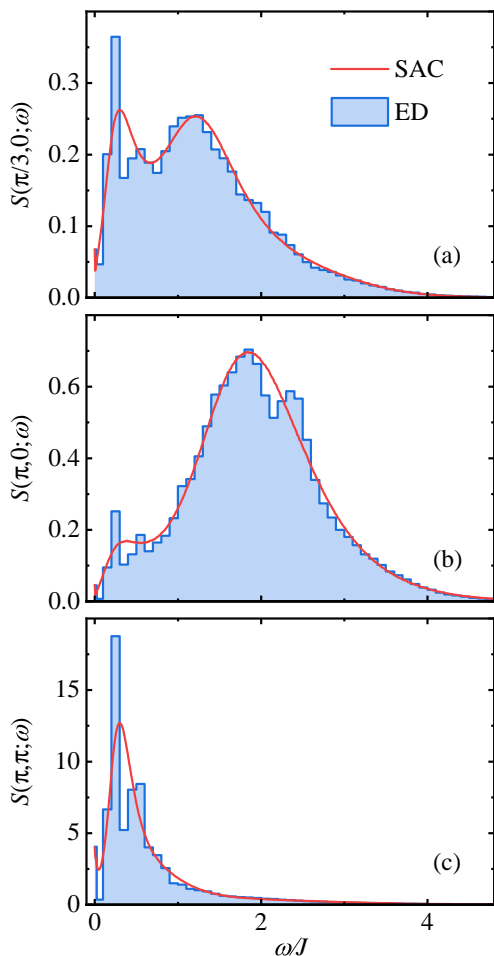


FIG. 30. Disorder averaged (1000 samples)  $S(\mathbf{q}, \omega)$  for system size  $L = 6$  diluted at  $p = 5/18$ , with only average sublattice balance;  $\langle N_A \rangle = \langle N_B \rangle = (1 - p)N/2$ . Results are shown at (a)  $\mathbf{q} = (\pi/3, 0)$ , (b)  $\mathbf{q} = (\pi, 0)$ , (c)  $\mathbf{q} = (\pi, \pi)$ . The histograms represent the distribution of  $\delta$  functions in the exact expression Eq. (4) and the red curves are the results of the SAC method applied to SSE data.

spectral functions in remarkable detail. Many other disordered spin models, in particular, should have interesting spectral features amenable to the same methods used here, e.g., other types of disordered 2D Heisenberg models [23, 26, 58–61] and the random  $J$ - $Q$  model [57].

## ACKNOWLEDGMENTS

We would like to thank Alexander Chernyshev, Wenan Guo, and Shiliang Li for valuable discussions, and also Ling Wang for help with the simulations of the dimer-monomer model. H.S. was supported by the National Natural Science Foundation of China under Grant No. 12122502, National Key Projects for Research and Development of China under Grant No. 2021YFA1400400, and by the Fundamental Research Funds for the Central Universities. A.W.S. was

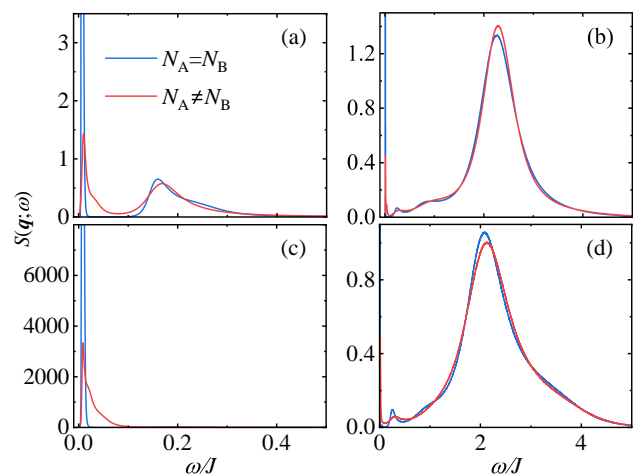


FIG. 31.  $S(\mathbf{q}, \omega)$  at representative  $\mathbf{q}$  points for  $p = 1/8$ ,  $L = 32$ . The blue and red curves show results in the balanced and unrestricted vacancy ensembles, respectively. The momentum is  $\mathbf{q} = (\pi/16, 0)$  in (a),  $\mathbf{q} = (\pi/2, \pi/2)$  in (b),  $\mathbf{q} = (\pi, \pi)$  in (c), and  $\mathbf{q} = (\pi, 0)$  in (d).

supported by the Simons Foundation under Grant No. 511064. Some of the numerical calculations were carried out on the Shared Computing Cluster managed by Boston University’s Research Computing Services.

## Appendix A: Sublattice imbalanced systems

In the main paper we have only shown results for systems with global sublattice balance;  $N_A = N_B$ . In a real 2D Heisenberg quantum magnet doped with non-magnetic impurities, this constraint would of course not be realistic requirement. Given that the individual clusters can be imbalanced even with global balance, the  $N_A = N_B$  and  $\langle N_A \rangle = \langle N_B \rangle$  ensembles should not be expected to differ in the thermodynamic limit. Nevertheless, we here show some results for systems where  $N_A = N_B$  was not imposed for each sample but  $\langle N_A \rangle = \langle N_B \rangle = (1 - p)N/2$ .

First, in Fig. 30 we show results analogous to Fig. 2, comparing SAC and exact Lanczos results for  $p = 5/18$  averaged over 1000 disorder samples. Here we observe that it is not possible to clearly distinguish the contributions from the rotor excitations. While there are low-energy peaks in the Lanczos based histograms at the same energy for all three momenta shown, there is much more spectral weight on the right hand side of this peak than in Fig. 2. The agreement between SAC and Lanczos results is also less impressive, though still acceptable, because of the difficulty in reproducing the shape of the shallow minimum between the two peaks.

In Fig. 31 we show SAC results for  $p = 1/8$ ,  $L = 32$ , comparing the two ensembles directly. At the two momenta close to the uniform and staggered wave-vectors,

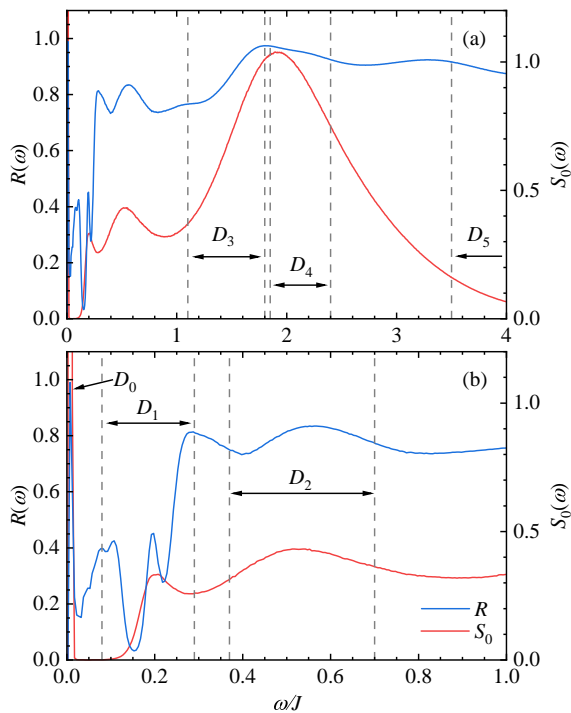


FIG. 32. Local spectral function for an individual  $L = 32$  vacancy realization at  $p = 1/16$  along with the frequency windows defining the maps  $D_0, \dots, D_5$  discussed in this Appendix. Corresponding results for the  $p = 1/8$  configuration used in Figs. 33 and 35 are shown in the main paper, Fig. 18.

Fig. 31(a) and Fig. 31(c), the rotor peak is again much more spread out in the unrestricted  $\langle N_A \rangle = \langle N_B \rangle$  ensemble. At the other two momenta, Fig. 31(b) and Fig. 31(d), the differences are rather small, but the unrestricted ensemble does not show the localization peak as clearly, again because of some spectral weight between it and the (now rather sharp) rotor peak. We fully expect the agreement between the two ensembles to improve as  $L$  is further increased.

### Appendix B: $L=32$ Real-space spectral maps

To complement the tomographic analysis of the real-space spectral weight in Secs. IVE and IVC, we here present additional results for  $L = 32$  vacancy realizations; one at  $p = 1/16$  and one at  $p = 1/8$ . The  $\mathbf{r}$  averaged quantity  $S_0(\omega)$  for  $p = 1/16$  (the analogue of the  $p = 1/8$  case in Fig. 18) is shown in Fig. 32 along with the windows used to define the integrals for the  $D_0, \dots, D_5$  in Eq. (15).

In Sec. IIE, we compared the monomer distribution with the rotor weight only for a system of size  $L = 16$  at  $p = 1/8$ . In Fig. 33 we show  $L = 32$  results for both  $p = 1/16$  and  $p = 1/8$ . In both cases, it is clear that sites with monomers correspond to elevated rotor weight, though there is some nonuniformity in the rotor weight

also among spins with no corresponding monomer occupation, especially some of the spins next to vacancies.

In Fig. 34 we show the tomographic maps  $D_1$ - $D_4$  for the  $L = 32$  configuration at  $p = 1/16$ , complementing the one for  $p = 1/8$  in Fig. 19. The energy windows are defined in Fig. 32. The spectral weight distributions are qualitatively similar to the  $p = 1/8$  case. Visually, there is a bit more variability in the spectral weight on the spins adjacent to vacancies in  $D_3$ , but this aspect of the low-energy magnons depend to some extent on how the energy window is chosen. The trend of spectral weight moving from the patches between vacancies to spins next to vacancies when the magnon energy is lowered from is a very stable feature for all the cases we have studied.

In the main paper we did not discuss the tomographic maps  $D_5$  corresponding to the high-energy tails of the spectral weight, within the frequency windows illustrated in Figs. 18 and 32 (which in both cases extend beyond the figure frames up to the highest frequencies of the tails of the distributions). Results for both  $p = 1/16$  and  $p = 1/8$  are shown in Fig. 35. Similar to the high-energy magnon dominated  $D_4$  map, the dominant spectral weight in  $D_5$  falls within the uniform patches between vacancies, with even less weight on the spins next to vacancies.

### Appendix C: Interacting dimer model

In Sec. IV we found that the simple dimer-monomer model was able to qualitatively explain the spread of quantum rotor weight in the form of peaks around  $\mathbf{q} = (0, 0)$  and  $(\pi, \pi)$ , but beyond these peaks the distribution is flat. It is then interesting to include interactions in the dimer-monomer model, which could potentially change the nature of the sublattice imbalance and produce more structure in  $\mathbf{q}$  space. Given our proposal that correlated singlet fluctuations are responsible for the observed structure, we here consider dimer-dimer interactions either favoring or disfavoring columnar order.

We use the partition functions

$$Z_{\pm} = \sum_{\mathcal{C}} \exp(\pm\beta \cdot N_p(\mathcal{C})), \quad (\text{C1})$$

where  $N_p(\mathcal{C})$  is the number of parallel dimers in configuration  $\mathcal{C}$ , i.e, the number of  $2 \times 2$  plaquettes with two dimers either horizontally or vertically oriented. We take the inverse temperature  $\beta$  to be large, so that the  $Z_+$  and  $Z_-$  system has the maximum and minimum number of parallel dimers, respectively. We again sample the configurations with minimal number of monomers for given vacancy realization.

In Fig. 36 we compare the previous noninteracting results for the specific vacancy realization in Fig. 6(a), here reproduced in Fig. 36(a) for convenience, with results for  $Z_+$  in Fig. 36(b) and for  $Z_-$  in Fig. 36(c). There are significant effects in the monomer distribution, with more

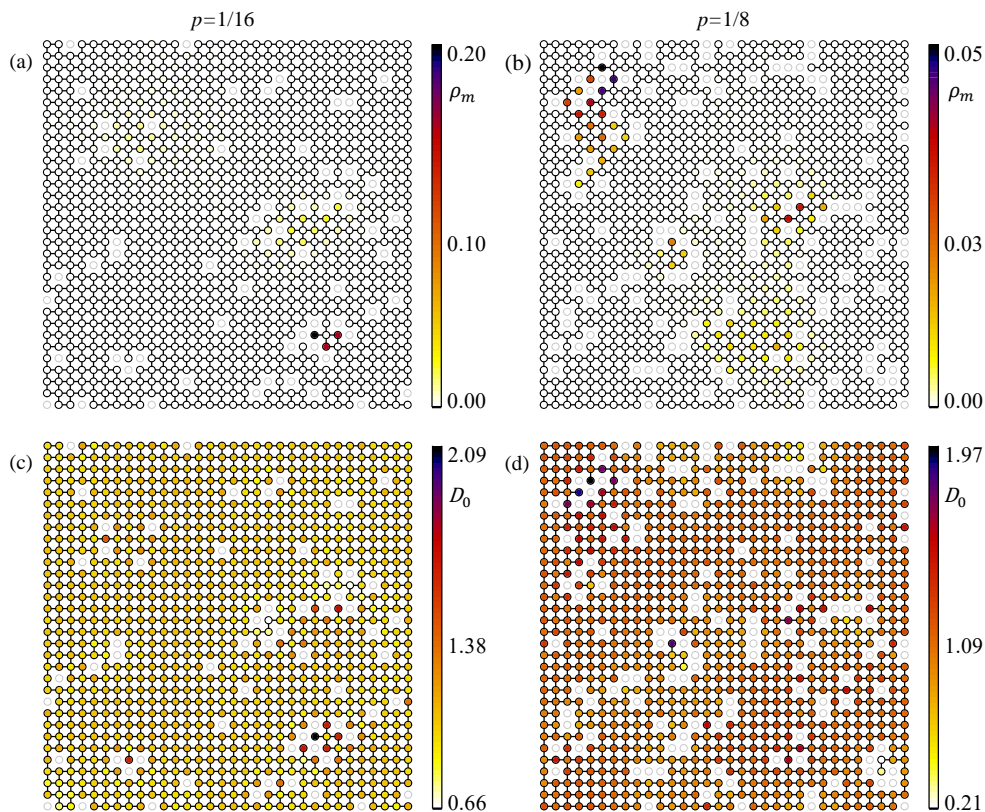


FIG. 33. Monomer distributions for  $L = 32$  systems with  $p = 1/8$  and  $p = 1/16$  are shown in (a) and (b) respectively. The tomographic quantum rotor weight distributions for the same samples are shown in (c) and (d).

parallel dimers leading to smaller areas of sublattice imbalance, while the suppression of parallel dimers cause larger regions.

An example of the rotor weight distribution computed as before using Eq. (24) is shown in Fig. 37. Here we only see small changes at the peaks relative to the noninteracting case for the repulsive model  $Z_-$ . For the attractive  $Z_+$  model, there are no detectable changes within statistical errors for this small system size. Thus, it seems unlikely that any classical dimer-monomer model would be able to describe the  $\mathbf{q}$  dependence of the rotor weight beyond the peaks at  $(0,0)$  and  $(\pi,\pi)$ . However, our results also show that those peaks are very robust, being

insensitive to the details of the model, even when the imbalanced regions themselves can vary strongly with the model parameters, as seen in Fig. 36. This result reinforces the notion that the peaks in the diluted Heisenberg model are indeed caused by local sublattice imbalance, even though the distribution of the “dangling spins” in the quantum model must differ from that of the monomers in the classical models. Given the previous results in Fig. 6 and the results with interactions included in Fig. 36, the non-interacting model is the best one in terms of matching the monomer distribution to the local magnetic response of the Heisenberg model.

- 
- [1] S.-W. Cheong, A. S. Cooper, L. W. Rupp, Jr., and B. Batlogg, Magnetic dilution study in  $\text{La}_2\text{CuO}_4$ : Comparison with other two-dimensional magnets, *Phys. Rev. B* **44**, 9739 (1991).
- [2] S. T. Ting, P. Pernambuco-Wise, J. E. Crow, E. Manousakis, and J. Weaver, Magnetic properties of  $\text{La}_2\text{Cu}_{1-x}\text{M}_x\text{O}_4$  with  $\text{M}=\text{Zn}$  and  $\text{Ni}$ , *Phys. Rev. B* **46**, 11772 (1992).
- [3] M. Corti, A. Rigamonti, F. Tabak, P. Carretta, F. Licci, and L. Raffo,  $^{139}\text{La}$  NQR relaxation and  $\mu\text{SR}$  study of Zn-doping effects in  $\text{La}_2\text{CuO}_4$  *Phys. Rev. B* **52**, 4226 (1995); Erratum *Phys. Rev. B* **53**, 2893 (1996).
- [4] P. Carretta, A. Rigamonti, and R. Sala, Spin dynamics in a two-dimensional disordered  $\text{S}=1/2$  Heisenberg paramagnet from  $^{63}\text{Cu}$  NQR relaxation in Zn-doped  $\text{La}_2\text{CuO}_4$ . *Phys. Rev. B* **55**, 3734 (1997).
- [5] O. P. Vajk, P. K. Mang, M. Greven, P. M. Gehring, and J. W. Lynn, Quantum Impurities in the Two-Dimensional Spin One-Half Heisenberg Antiferromagnet, *Science* **295**, 1691 (2002).
- [6] N. Papinutto, P. Carretta, S. Gonthier, and P. Millet Spin dilution in frustrated two-dimensional  $\text{S}=1/2$  anti-



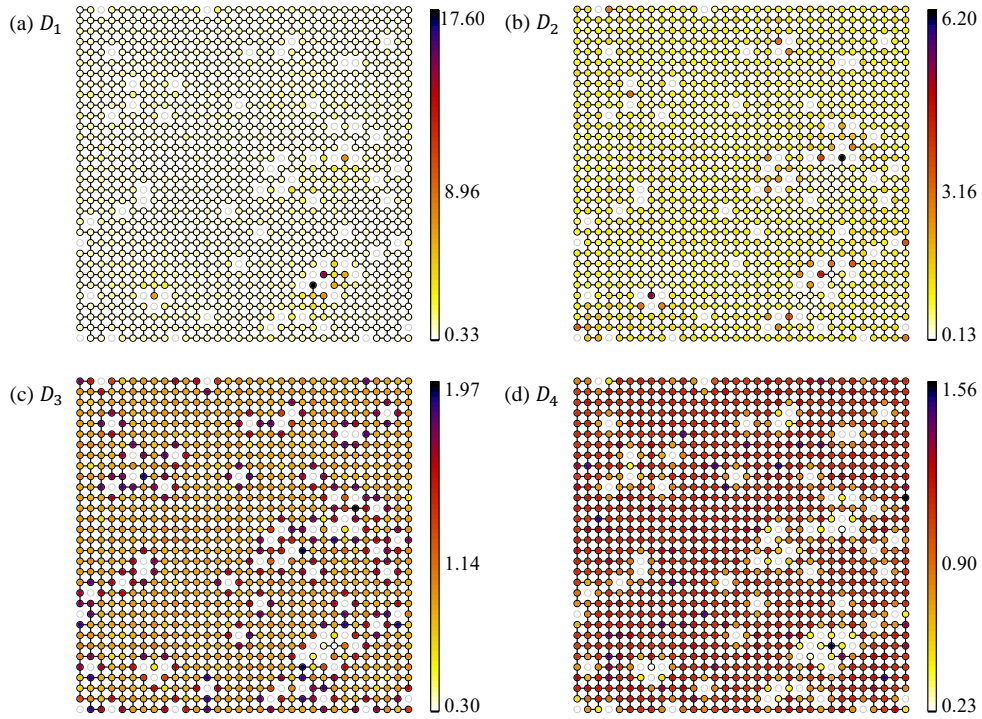


FIG. 34. Tomographic maps  $D_1, \dots, D_4$  for the same  $p = 1/16$  samples as in Figs. 33(a) and 33(c). The maps for the same  $p = 1/8$  samples as in Figs. 33(b) and 33(d) are shown in Fig. 19.

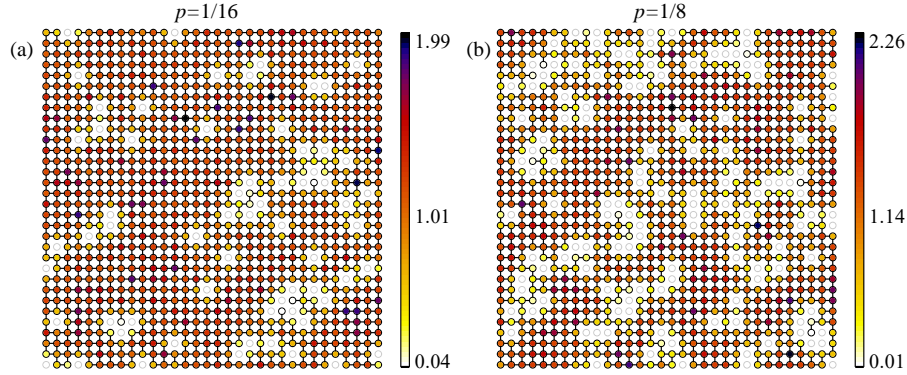


FIG. 35. Tomographic maps  $D_5$  corresponding to the high energy tails of the same vacancy samples as in Fig. 33. The energy windows are shown in Figs. 18 and 32.

- ferromagnets on a square lattice, Phys. Rev. B **71**, 174425 (2005).
- [7] A. B. Harris and S. Kirkpatrick, Low-frequency response functions of random magnetic systems, Phys. Rev. B **16**, 542 (1977).
- [8] N. Bulut, D. Hone, D. J. Scalapino, and E. Y. Loh, Static vacancies on a 2D Heisenberg spin-1/2 antiferromagnet, Phys. Rev. Lett. **62**, 2192 (1989).
- [9] W. Brenig and A. P. Kampf, Spin excitations in a quantum antiferromagnet with magnetic impurities and vacancies, Phys. Rev. B **43**, 12914 (1991).
- [10] C. C. Wan and A. B. Harris, and D. Kumar, Heisenberg antiferromagnet with a low concentration of static defects, Phys. Rev. B **48**, 1036 (1993).
- [11] C. Yasuda and A. Oguchi, J. Phys. Soc. Jpn. **66**, 2836 (1997).
- [12] C. Yasuda and A. Oguchi, J. Phys. Soc. Jpn. **68**, 2773 (1999).
- [13] Y.-C. Chen and A. H. Castro Neto, Effective field theory for layered quantum antiferromagnets with nonmagnetic impurities, Phys. Rev. B **61**, R3772 (2000).
- [14] A. L. Chernyshev, Y. C. Chen, and A. H. Castro Neto, Long-Range Order and Low-Energy Spectrum of Diluted 2D Quantum Antiferromagnet, Phys. Rev. Lett. **87**, 067209 (2001).
- [15] A. L. Chernyshev, Y. C. Chen, and A. H. Castro Neto, Diluted quantum antiferromagnets: Spin excitations and long-range order, Phys. Rev. B **65**, 104407 (2002).
- [16] E. R. Mucciolo, A. H. Castro Neto, and C. Chamon, Excitations and quantum fluctuations in site-diluted two-

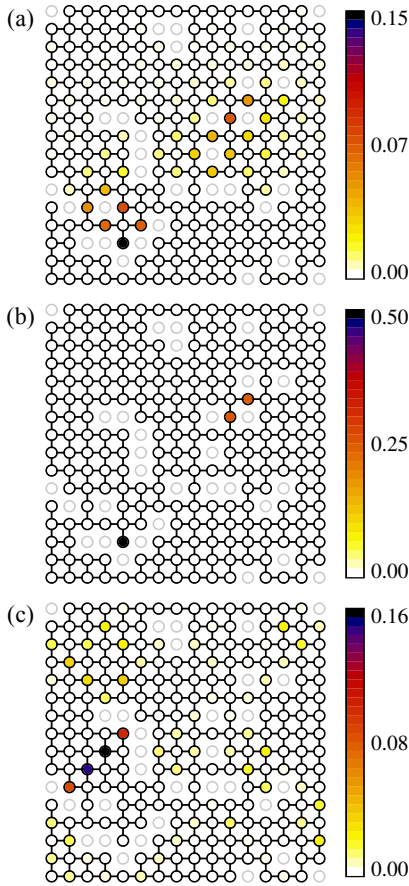


FIG. 36. Monomer distribution in the system previously considered with the noninteracting dimer-monomer model in Fig. 6(a), here repeated in (a). In (b) and (c), results are shown for the interacting models in Eq. (C1);  $Z_+$  (favoring parallel dimers) and  $Z_-$  (disfavoring parallel dimers).

dimensional antiferromagnets Phys. Rev. B **69**, 214424 (2004).

- [17] C.-W. Liu, S. Liu, Y.-J. Kao, A. L. Chernyshev, and A. W. Sandvik, Impurity-Induced Frustration in Correlated Oxides, Phys. Rev. Lett. **102**, 167201 (2009).
- [18] S. Liu and A. L. Chernyshev, Impurity-induced frustration: Low-energy model of diluted oxides, Phys. Rev. B **87**, 064415 (2013).
- [19] E. Manousakis, Spin correlations in a two-dimensional Heisenberg antiferromagnet doped with static holes, Phys. Rev. B **45**, 7570 (1992).
- [20] K. Kato, S. Todo, K. Harada, N. Kawashima, S. Miyashita, and H. Takayama, Quantum Phase Transition of the Randomly Diluted Heisenberg Antiferromagnet on a Square Lattice Phys. Rev. Lett. **84**, 4204 (2000).
- [21] A. W. Sandvik, Classical percolation transition in the diluted two-dimensional  $S=1/2$  Heisenberg antiferromagnet, Phys. Rev. B **66**, 024418 (2002).
- [22] K. H. Höglund and A. W. Sandvik, Impurity effects at finite temperature in the two-dimensional  $S=1/2$  Heisenberg antiferromagnet, Phys. Rev. B **70**, 024406 (2004).
- [23] R. Yu, T. Roscilde, and S. Haas, Quantum Percolation in Two-Dimensional Antiferromagnets, Phys. Rev. Lett.

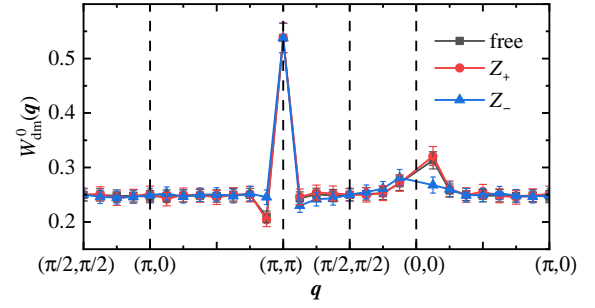


FIG. 37. Rotor weight distribution  $W_{\text{dm}}^0(\mathbf{q})$  along a cut in the BZ based on simulations of the noninteracting dimer model (black squares) as well as the interacting models  $Z_+$  (red circles) and  $Z_-$  (blue triangles) for system size  $L = 16$  at  $p = 1/8$ , averaged over 2000 vacancy samples, each constrained to have two monomers.

**94**, 197204 (2005).

- [24] A. Lüscher and O. P. Sushkov, Long-range dynamics of magnetic impurities coupled to a two-dimensional Heisenberg antiferromagnet Phys. Rev. B **71**, 064414 (2005).
- [25] F. Anfuso and S. Eggert, Knight Shifts around Vacancies in the 2D Heisenberg Model, Phys. Rev. Lett. **96**, 017204 (2006)
- [26] R. Yu, T. Roscilde, and S. Haas, Quantum disorder and Griffiths singularities in bond-diluted two-dimensional Heisenberg antiferromagnets, Phys. Rev. B **73**, 064406 (2006).
- [27] L. Wang and A. W. Sandvik, Low-Energy Dynamics of the Two-Dimensional  $S=1/2$  Heisenberg Antiferromagnet on Percolating Clusters, Phys. Rev. Lett. **97**, 117204 (2006);
- [28] L. Wang and A. W. Sandvik, Low-energy excitations of two-dimensional diluted Heisenberg quantum antiferromagnets, Phys. Rev. B **81**, 054417 (2010).
- [29] H. J. Changlani, S. Ghosh, S. Pujari, and C. L. Henley, Emergent Spin Excitations in a Bethe Lattice at Percolation, Phys. Rev. Lett. **111**, 157201 (2013).
- [30] P. Weinberg and A. W. Sandvik, Dynamic scaling of the restoration of rotational symmetry in Heisenberg quantum antiferromagnets Phys. Rev. B **96**, 054442 (2017).
- [31] R. Bhola, S. Biswas, M. M. Islam, and K. Damle, Dulmage-Mendelsohn Percolation: Geometry of Maximally Packed Dimer Models and Topologically Protected Zero Modes on Site-Diluted Bipartite Lattices, Phys. Rev. X **12**, 021058 (2022).
- [32] H. Shao, and A. W. Sandvik, Progress on stochastic analytic continuation of quantum Monte Carlo data, Phys. Rep. **1003** 1–88 (2023).
- [33] R. R. P. Singh and M. P. Gelfand, Spin-Wave Excitation-Spectra and Spectral Weights in Square Lattice Antiferromagnets, Phys. Rev. B **52**, 15695(R) (1995).
- [34] A. W. Sandvik and R. R. P. Singh, High-Energy Magnon Dispersion and Multimagnon Continuum in the Two-Dimensional Heisenberg Antiferromagnet, Phys. Rev. Lett. **86**, 528 (2001).
- [35] B. Dalla Piazza, M. Mourigal, N. B. Christensen, G. J. Nilsen, P. Tregenna-Piggott, T.G. Perring, M. Enderle, D. F. McMorrow, D. A. Ivanov, and H. M. Rønnow, Fractional Excitations in the Square-Lattice Quantum

- Antiferromagnet, *Nat. Phys.* **11**, 62 (2015).
- [36] H. Shao, Y. Q. Qin, S. Capponi, S. Chesi, Z. Y. Meng, and A. W. Sandvik, Nearly Deconfined Spinon Excitations in the Square-Lattice Spin-1/2 Heisenberg Antiferromagnet, *Phys. Rev. X* **7**, 041072 (2017).
- [37] M. Powalski, K. P. Schmidt, G. S. Uhrig, Mutually attracting spin waves in the square-lattice quantum antiferromagnet, *SciPost Phys.* **4**, 001 (2018)
- [38] H. J. Changlani, S. Ghosh, C. L. Henley, and A. M. Läuchli, Heisenberg antiferromagnet on Cayley trees: Low-energy spectrum and even/odd site imbalance, *Phys. Rev. B* **87**, 085107 (2013).
- [39] S. Ghosh, H. J. Changlani, and C. L. Henley, Schwinger boson mean field perspective on emergent spins in diluted Heisenberg antiferromagnets, *Phys. Rev. B* **92**, 064401 (2015).
- [40] A. W. Sandvik, Evidence for Deconfined Quantum Criticality in a Two-Dimensional Heisenberg Model with Four-Spin Interactions, *Phys. Rev. Lett.* **98**, 227202 (2007).
- [41] E. Dagotto, Correlated electrons in high-temperature superconductors, *Rev. Mod. Phys.* **66**, 763 (1994).
- [42] A. W. Sandvik, Stochastic series expansion method with operator-loop update *Phys. Rev. B* **59**, R14157 (1999).
- [43] A. W. Sandvik, Computational Studies of Quantum Spin Systems, *AIP Conf. Proc.* **1297**, 135 (2010).
- [44] A. W. Sandvik, Stochastic Series Expansion Methods, in *Many-Body Methods for Real Materials, Modeling and Simulation, Volume 9*, Edited by E. Pavarini, E. Koch, and S. Zhang (Schriften des Forschungszentrums Jülich, 2019).
- [45] A. W. Sandvik, Quantum Monte Carlo in the interaction representation: Application to a spin-Peierls model, *Phys. Rev. B* **56**, 14510 (1997).
- [46] M. Jarrell and J. E. Gubernatis, Bayesian inference and the analytic continuation of imaginary-time quantum Monte Carlo data, *Phys. Rep.* **269**, 133 (1996).
- [47] G. Schumm, S. Yang, and A. W. Sandvik, Cross Validation in Stochastic Analytic Continuation, [arXiv:2406.06763](https://arxiv.org/abs/2406.06763).
- [48] K. Ghanem and E. Koch, Generalized maximum entropy methods as limits of the average spectrum method, *Phys. Rev. B* **108**, L201107 (2023).
- [49] K. S. D. Beach, Identifying the maximum entropy method as a special limit of stochastic analytic continuation, [arXiv:cond-mat/0403055](https://arxiv.org/abs/cond-mat/0403055).
- [50] P. W. Anderson, An Approximate Quantum Theory of the Antiferromagnetic Ground State, *Phys. Rev.* **86**, 694 (1952).
- [51] E. Manousakis, The spin-1/2 Heisenberg antiferromagnet on a square lattice and its application to the cuprous oxides, *Rev. Mod. Phys.* **63**, 1 (1991).
- [52] A. W. Sandvik, A generalization of Handscomb's quantum Monte Carlo scheme—application to the 1D Hubbard model, *J. Phys A: Math. Gen.* **25** (1992).
- [53] R. R. P. Singh and D. A. Huse, Microscopic calculation of the spin-stiffness constant for the spin-1/2 square-lattice Heisenberg antiferromagnet, *Phys. Rev. B* **40**, 7247 (1989).
- [54] O. A. Starykh, A. W. Sandvik, and R. R. P. Singh, Dynamics of the spin 1/2 Heisenberg chain at intermediate temperatures, *Phys. Rev. B* **55**, 14953 (1997).
- [55] Y. R. Shu, M. Dupont, D. X. Yao, S. Capponi, and A. W. Sandvik, Dynamical properties of the S=1/2 random Heisenberg chain, *Phys. Rev. B* **97**, 104424 (2018).
- [56] R. K. Kaul, R. G. Melko, M. A. Metlitski, and S. Sachdev, Imaging Bond Order near Nonmagnetic Impurities in Square-Lattice Antiferromagnets *Phys. Rev. Lett.* **101**, 187206 (2008).
- [57] L. Liu, H. Shao, Y.-C. Lin, W. Guo, and A. W. Sandvik, Random-Singlet Phase in Disordered Two-Dimensional Quantum Magnets *Phys. Rev. X* **8**, 041040 (2018).
- [58] T. Roscilde and S. Haas, Quantum Localization in Bilayer Heisenberg Antiferromagnets with Site Dilution, *Phys. Rev. Lett.* **95**, 207206 (2005)
- [59] A. W. Sandvik, Quantum Criticality and Percolation in Dimer-Diluted Two-Dimensional Antiferromagnets, *Phys. Rev. Lett.* **96**, 207201 (2006).
- [60] N. Laflorencie, S. Wessel, A. Läuchli, and H. Rieger, Random-exchange quantum Heisenberg antiferromagnets on a square lattice, *Phys. Rev. B* **73**, 060403(R) (2006).
- [61] R. Yu, O. Nohadani, S. Haas, and T. Roscilde, Magnetic Bose glass phases of coupled antiferromagnetic dimers with site dilution, *Phys. Rev. B* **82**, 134437 (2010).
- [62] J.-Y. P. Delannoy, M. J. P. Gingras, P. C. W. Holdsworth, and A.-M. S. Tremblay, Low-energy theory of the  $t$ - $t'$ - $t''$ - $U$  Hubbard model at half-filling: Interaction strengths in cuprate superconductors and an effective spin-only description of  $\text{La}_2\text{CuO}_4$ , *Phys. Rev. B* **79**, 235130 (2009).
- [63] J.-Y. P. Delannoy, A. G. Del Maestro, M. J. P. Gingras, and P. C. W. Holdsworth, Site dilution in the half-filled one-band Hubbard model: Ring exchange, charge fluctuations, and application to  $\text{La}_2\text{Cu}_{1-x}(\text{Mg}/\text{Zn})_x\text{O}_4$ , *Phys. Rev. B* **79**, 224414 (2009).